Icarus 210 (2010) 742–762

Contents lists available at ScienceDirect

Icarus

journal homepage: www.elsevier.com/locate/icarus

Persistent rings in and around Jupiter's anticyclones – Observations and theory

Imke de Pater [a,*], Michael H. Wong [a], Philip Marcus [b], Statia Luszcz-Cook [a], Maté Ádámkovics [a], Al Conrad [c], Xylar Asay-Davis [d], Christopher Go [e]

[a] Astronomy Department, 601 Campbell Hall, University of California, Berkeley, CA 94720, United States
[b] Department of Mechanical Engineering, Program of Applied Science & Technology, University of California, Berkeley, CA 94720, United States
[c] W.M. Keck Observatory, Waimea, HI 96743, United States
[d] Center for Nonlinear Studies, Los Alamos National Laboratory, Los Alamos, NM 87545, United States
[e] Physics Department, University of San Carlos, Nasipit, Talamban, Cebu City, Philippines

ARTICLE INFO

Article history:
Received 22 October 2009
Revised 28 July 2010
Accepted 30 July 2010
Available online 10 August 2010

Keywords:
Jupiter, Atmosphere
Hubble Space Telescope observations
Infrared observations
Adaptive optics

ABSTRACT

We present observations and theoretical calculations to derive the vertical structure of and secondary circulation in jovian vortices, a necessary piece of information to ultimately explain the red color in the annular ring inside Jupiter's Oval BA. The observations were taken with the near-infrared detector NIRC2 coupled to the adaptive optics system on the 10-m W.M. Keck telescope (UT 21 July 2006; UT 11 May 2008) and with the Hubble Space Telescope at visible wavelengths (UT 24 and 25 April 2006 using ACS; UT 9 and 10 May 2008 using WFPC2). The spatial resolution in the near-IR (~0.1–0.15″ at 1–5 μm) is comparable to that obtained at UV–visible wavelengths (~0.05–0.1″ at 250–890 nm). At 5 μm we are sensitive to Jupiter's thermal emission, whereas at shorter wavelengths we view the planet in reflected sunlight. These datasets are complementary, as images at 0.25–1.8 μm provide information on the clouds/hazes in the troposphere–stratosphere, while the 5-μm emission maps yield information on deeper layers in the atmosphere, in regions without clouds. At the latter wavelength numerous tiny ovals can be discerned at latitudes between ~45°S and 60°S, which show up as rings with diameters $\lesssim$1000 km surrounding small ovals visible in HST data. Several white ovals at 41°S, as well as a new red oval that was discovered to the west of the GRS, also reveal 5-μm bright rings around their peripheries, which coincide with dark/blue rings at visible wavelengths. Typical brightness temperatures in these 5-μm bright rings are 225–250 K, indicative of regions that are cloud-free down to at least the ~4 bar level, and perhaps down to 5–7 bar, i.e., well within the water cloud.

Radiative transfer modeling of the 1–2 μm observations indicates that all ovals, i.e., including the Great Red Spot (GRS), Red Oval BA, and the white ovals at 41°S, are overall very similar in vertical structure. The main distinction between the ovals is caused by variations in the particle densities in the tropospheric–stratospheric hazes (2–650 mbar). These are 5–8 times higher above the red ovals than above the white ones at 41°S. The combination of the 5-μm rings and the vertical structure derived from near-IR data suggests anticyclones to extend vertically from (at least) the water cloud (~5 bar) up to the tropopause (~100–200 mbar), and in some cases into the stratosphere.

Based upon our observations, we propose that air is rising along the center of a vortex, and descending around the outer periphery, producing the 5-μm bright rings. Observationally, we constrain the maximum radius of these rings to be less than twice the local Rossby deformation radius, L_R. If the radius of the visible oval (i.e., the clouds that make the oval visible) is >3000 km, our observations suggest that the descending part of the secondary circulation must be within these ovals. For the Red Oval BA, we postulate that the return flow is at the location of its red annulus, which has a radius of ~3000 km.

We develop a theory for the secondary circulation, where air is (baroclinically) rising along the center of a vortex in a subadiabatic atmosphere, and descending at a distance not exceeding ~2× the local Rossby deformation radius. Using this model, we find a timescale for mixing throughout the vortex of order several months, which suggests that the chromophores that are responsible for the red color of Oval BA's red annulus must be produced locally, at the location of the annulus. This production most likely results from the adiabatic heating in the descending part of the secondary circulation. Such higher-than-ambient temperature causes NH_3–ice to sublime, which will expose the condensation nuclei, such as the red chromophores.

* Corresponding author. Fax: +1 510 642 3411.
E-mail address: imke@berkeley.edu (I. de Pater).

0019-1035/$ - see front matter © 2010 Elsevier Inc. All rights reserved.
doi:10.1016/j.icarus.2010.07.027

1. Introduction

At the time of the Voyager flyby in 1979 Jupiter was characterized as a planet with white zones and brown belts. In addition, the Great Red Spot (GRS) and three white ovals featured prominently on Jupiter's disk. Observations of the GRS may trace back to 1665, and the white ovals have been seen since the 1930s (Peek, 1958). These ovals were in a stable configuration known as a "Kármán vortex street", where anticyclones are staggered with cyclones (Youssef and Marcus, 2003). Between 1998 and 2000 the white ovals merged and by 2000 only one of them was left, Oval BA (Sanchez-Lavega et al., 1999, 2001). About 5–6 years later, in December 2005, this Oval BA turned red (Go et al., 2006). A color change of a vortex as long-lived or as large as Oval BA is without precedent, and the cause of this color change is not understood.

After the announcement of Oval BA's change in color from white to red, we received director's discretionary time to observe Jupiter with the Hubble Space Telescope (HST; GO/DD 10782) on UT 16, 24 and 25 April 2006. Observations through different filters were obtained to: (i) determine the altitude of the clouds in the GRS and Red Oval BA and (ii) extract velocity fields for the GRS and Red Oval BA. Several groups have analyzed these data in a variety of ways, as summarized below.

1.1. Oval BA: previous results

Simon-Miller et al. (2006) show that the only observable change for Oval BA between 2005 and 2006 appeared to be an increase in the 435 nm absorption. Such an increase in the absorption of blue light would naturally lead to a reddening. Using HST methane band (~890 nm) images from 1995 to 2009, Wong et al. (2010) argue that the distribution of upper tropospheric haze in the oval remained unchanged during this entire period, regardless of the mergers and the color change. Using detailed radiative transfer calculations to model the reflectivity (I/F) in HST data from 2005 and 2006 at six different wavelengths, Pérez-Hoyos et al. (2009) show that the vertical structure of the cloud/haze properties in Oval BA did not change during the reddening period. Asay-Davis et al. (2009) developed new algorithms to extract wind velocities from high resolution images taken tens of minutes to tens of hours apart. They show that the velocity fields of Oval BA were nearly the same in 2000 when the oval was white (using Cassini data), and in 2006 when it was red (using HST data). Similar results, i.e., no change in Oval BA's wind velocity field, were obtained by Hueso et al. (2009) between 2000 and 2007 (they included the New Horizons data). Without a change in Oval BA's upper tropospheric/stratospheric hazes or its wind field, it is hard to explain its reddening. Simon-Miller et al. (2006) and Cheng et al. (2008) did report large changes in the *maximum* wind speeds. However, a comparison of the *entire* or *average* velocity fields as in Asay-Davis et al. (2009) and Hueso et al. (2009) gives a better characterization of the physical conditions of the vortices than comparing values out in the tail of the velocity distribution.

A red color is usually attributed to red "chromophores". As discussed by West et al. (1986), the two leading models for any red color in Jupiter's atmosphere are: (i) "Hiding" and "exposing" red chromophores, where the chromophores act as condensation nuclei. If the temperature is below the condensation temperature of ammonia, NH_3-gas may condense onto these chromophores, "hiding" the original particulates. When the temperature rises above this level, the ice will sublime and "expose" the original chromophore. (ii) Photochemical production of red chromophores, a process that starts with photolysis of PH_3 and/or NH_4SH in the upper troposphere, after being dredged up from deeper levels. Photodissociation is most effective at high altitudes ($P < 300$ mbar). After a series of complex chemical reactions, the photochemical products may be transformed into small (perhaps red) particulates, which we refer to as chromophores.

Simon-Miller et al. (2006) and Pérez-Hoyos et al. (2009) suggest that the chromophores, or the precursors of such chromophores (such as NH_4SH particles), which produce the red color in Oval BA may be dredged up from deeper down, in which case one might expect the center of the oval to redden first (assuming gas is rising along the central axis). Subsequent mixing would distribute the chromophores evenly throughout the oval, on a timescale that depends on the radial velocity. However, one of the most intriguing observations of Red Oval BA is that its red color is confined to a ring around the core, and this red annulus has been stable for over 4 years, despite two passages with the GRS. Such passages add strain on the vortices, which presumably would accelerate the mixing. The outer edge of the red annulus coincides with the contour of peak velocity, which corresponds approximately to the outer edge of the potential vorticity anomaly of Oval BA (Asay-Davis et al., 2009).

1.2. Hypothesis

Marcus et al. (2007) suggest that the red color of Oval BA is tied in with a secondary (vertical) circulation pattern within the oval, where gases rise up along the center of the oval, and descend at the approximate location of the red ring. Adiabatic compression at this location leads to a temperature increase, which can explain the red color of the annulus using either one of West et al.'s (1986) mechanisms—as both the NH_3 saturation vapor pressure and the chemical pathways that produce the particulates after the original compounds are destroyed via photodissociation, are strongly temperature dependent. Hence, this mechanism suggests that the red color is produced locally, and that its location is determined dynamically.

Our goal in this paper is to test the secondary circulation hypothesis of Marcus et al. (2007) and determine the cause of the oval's red color. To reach this goal, we need to show: (1) the existence of a secondary circulation pattern within Oval BA and (2) re-evaluate the radial mixing time for chromophores.

We investigate the secondary circulation in Oval BA via a combined analysis of visible wavelength HST observations and Keck adaptive optics images at wavelengths between 1 and 5 μm. With these data we derive and intercompare the vertical structure of several differently sized ovals, which gives us, observationally, a handle on the secondary circulation (our derived schematic of the circulation is shown in Fig. 16a and b). The observations conducted for this goal are described in summarizes the results of Jupiter as seen in reflected sunlight, and Section 4 shows the results of Jupiter's 5-μm thermal emission.

In order to tie the circulation model for Oval BA to the mechanism that produces the red color in the red annulus, we need to estimate the timescale of radial mixing. Unfortunately, as errorbars in wind velocity fields are of order ~5 m/s (Asay-Davis et al., 2009), it is impossible to determine the radial mixing time observationally, unless the radial velocities are of order tens of m/s; as radial velocities have not been detected, it must be less than ~5 m/s. So we have to rely on theoretical calculations to determine the timescale for mixing. The only estimate for radial mixing that we found in the literature is that by Conrath et al. (1981). From the measured temperature contrast across the GRS, these authors derive a typical radial velocity of order 1 cm/s (at the tropopause), which implies that the timescales for radial spreading (~years–decade) may exceed those of radiative cooling, the latter being of order 4–5 years at the tropopause (Conrath et al., 1990). Hence, if these timescales are right, mixing of material throughout the vortex cannot be detected on timescales less than a few years. In Section 5.1 we re-evaluate Conrath et al.'s (1981) calculations, in particular the vertical temperature gradient used by them, and find timescales

for mixing that are ~100 times faster. We find radial velocities of order ~1 m/s, and hence the mixing time of material that moves passively within Oval BA, including any red particulates that initially appeared in the annulus, is of order months, rather than a decade. Such a short mixing time leads us to conclude that the red chromophores in Oval BA must be produced locally, as outlined in Section 5.2. For comparison we discuss the vertical structure and secondary circulation theory of smaller ovals in Section 5.1, and the GRS in Section 5.3; our overall conclusions are summarized in Section 6.

2. Observations and data reduction

2.1. Keck adaptive optics (AO) observations

We observed Jupiter with the 10-m W.M. Keck II telescope on Mauna Kea, Hawaii, on UT 21 July 2006 and 11 May 2008. We used the near-infrared camera, NIRC2, a 1024 × 1024 Aladdin-3 InSb array coupled to the AO system, to observe the planet when both the GRS and Red Oval BA were visible. We used both NIRC2's wide-field and narrow-field cameras. The wide-field camera has a plate scale of 39.69 mass per pixel and covers a field ~40″ × 40″; the narrow-field camera, with 9.94 mass pixels, covers ~10″ × 10″. The narrow camera over-samples all wavelengths sensed by NIRC2 (~1.2–5 μm), and can therefore provide angular resolution near the diffraction limit in all filters, but can cover only a portion of Jupiter's surface. On the other hand, the wide camera covers most of Jupiter's surface in a single image, but under-samples the shorter wavelengths (~1–2.5 μm), and saturates at the longer wavelengths (~3–5 μm).

Since Jupiter is too large to be used for wavefront sensing, we had selected dates when one or more of the Galilean moons would be nearby to serve either as a tip-tilt "star" in conjunction with the laser (LGS – Laser Guide Star), or as a Natural Guide Star (NGS) for direct wavefront sensing. The guide star limiting magnitude for LGS is 18th magnitude at visible wavelengths (V_{mag}), while NGS guide stars must be brighter than $V_{mag} = 15$. The guide stars used for these observations (Io, Europa, and Ganymede) were approximately 5–6th V_{mag}, and so well within these limits. However, the high background near Jupiter's limb affects the observations. We determined that the moons Amalthea (~14th V_{mag}) and Thebe (15–16th V_{mag}), though bright enough in principle, are "lost" in Jupiter's scattered light, and cannot be used for wavefront sensing.

Since NGS-AO observations require a guide star within ~30″ from the target, observations can only be carried out over a limited amount of time, typically no longer than 30–45 min. With LGS-AO, the tip-tilt star can be up to ~60″ from the target, which more than doubles the time accessible for AO observing. Moreover, since we are interested in targeting a feature on Jupiter's disk, the larger 60″ "throw" available with LGS (over NGS) also provides additional flexibility in scheduling the observation, since the feature can be further away from that limb of the planet that is closest to the guide star. Examples of our LGS and NGS set-ups are shown in Fig. 1. In the LGS set-up (panel (a)), a large fraction of Jupiter can be viewed on the wide camera, including the GRS and Red Oval BA (red diamonds); the GRS and red oval are not (yet) visible in the narrow camera. Ganymede was chosen here as tip-tilt star. Panel (b) shows the configuration for the NGS-AO observations conducted later that evening, when Europa became visible and Ganymede had moved too far from Jupiter to serve as tip-tilt star for the LGS system. Since Europa is much brighter than the artificial laser "star" (5.6 vs. 10th V_{mag}), Europa can be used as a natural guide star much closer to Jupiter's limb than the laser. We determined that the laser has to be $\gtrsim 15''$ off the limb of Jupiter to avoid introducing a gradient across the wavefront sensor due to Jupiter's scattered light.

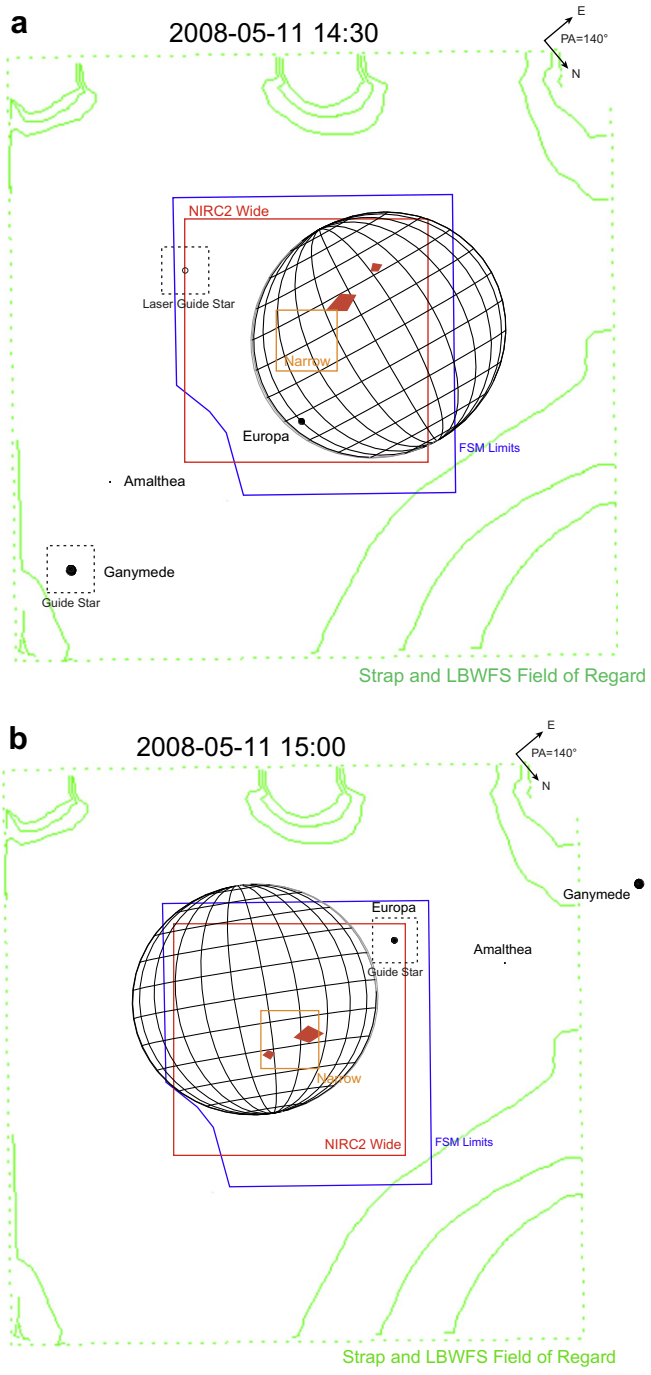

Fig. 1. Examples of our planning tools for the Keck AO observations on 11 May 2008, for (a) the LGS-AO set-up, and (b) the NGS-AO set-up. The NIRC2 wide-field camera is shown by the large red box; the narrow camera by the small orange box. Both cameras are centered at the same place. The larger (blue) box indicates the mechanical limits of the probe used to acquire the guide star when operating in NGS mode. The dotted-green box indicates the mechanical limits of the probe used to acquire the tip-tilt star in LGS mode, while the laser must be located within the blue box. The dotted-green box is larger by design. This is possible because a tip-tilt reference can be further from the object of study than the beacon used to measure the wavefront, and in LGS mode the tip-tilt star is separated from the laser. The green contours indicate vignetted regions which must be avoided for tip-tilt stars. In (a) Ganymede is chosen as tip-tilt star, with the laser for wavefront sensing; in (b) Europa serves both as our natural tip-tilt and wavefront-star. Jupiter with the GRS and Oval BA (red diamonds) is indicated. (For interpretation of the references to color in this figure legend, the reader is referred to the web version of this article.)

A summary of the Keck observations is provided in Table 1. Since our guide stars were offset from the center of Jupiter by

Table 1
Keck observations with the NIRC2 camera.

Date (UT) h:m:s	Filter	λ (μm)	$\Delta\lambda$ (μm)	$N \times$ Tint (s)	# Frames	NGS/LGS[a]	Satellite[b]	Offset[c]	I/F[d]
2006-07-21 06:39:53	hcont	1.580	0.023	10 × 0.18	1	LGS	Io	44.1	
2006-07-21 07:13:26	hcont	1.580	0.023	10 × 0.18	3	NGS	Io	35.4	0.80
2006-07-21 07:15:15	feii	1.646	0.026	10 × 0.18	3	NGS	Io	35.0	0.77
2006-07-21 07:26:53	Ms	4.670	0.241	20 × 0.18	3	NGS	Io	31.9	
2006-07-21 07:32:11	hcont	1.580	0.023	20 × 0.18	3	NGS	Io	30.6	0.80
2006-07-21 07:33:30	feii	1.646	0.026	20 × 0.18	3	NGS	Io	30.2	0.77
2006-07-21 07:34:59	pabeta	1.290	0.019	20 × 0.18	3	NGS	Io	29.8	0.85
2006-07-21 07:39:37	Ms	4.670	0.241	20 × 0.18	3	NGS	Io	28.6	
2008-05-11 14:46:37	hcont	1.580	0.023	10 × 0.18	4	LGS	Ganymede	66.7	
2008-05-11 14:48:49	feii	1.646	0.026	10 × 0.18	4	LGS	Ganymede	67.2	
2008-05-11 14:50:35	pabeta	1.290	0.019	10 × 0.18	4	LGS	Ganymede	67.5	
2008-05-11 15:02:30	pabeta	1.290	0.019	10 × 0.18	3	NGS	Europa	26.7	0.63
2008-05-11 15:03:54	hcont	1.580	0.023	10 × 0.18	3	NGS	Europa	27.1	0.33
2008-05-11 15:05:03	feii	1.646	0.026	10 × 0.18	3	NGS	Europa	27.3	0.33
2008-05-11 15:06:15	jcont	1.213	0.020	10 × 0.18	3	NGS	Europa	27.6	0.60
2008-05-11 15:09:48	Ms	4.670	0.241	20 × 0.18	12	NGS	Europa	28.5–31.9	

All observations were carried out with the WIDE camera, except for Ms where the NARROW camera was used.
[a] Natural Guide Star (NGS), Laser Guide Star (LGS).
[b] Satellite used for tip-tilt (LGS) or wavefront sensing (NGS).
[c] Offset satellite from center of Jupiter (″).
[d] Disk-averaged I/F of the satellite, as measured in images that contain both Jupiter and the satellite.

Table 2
Keck calibration stars.

Date (UT)	Calibrator	Filter	Magnitude	Flux density (ergs s^{-1} cm^{-2} μm^{-1})
2006-07-21	SJ9160	hcont	10.701	6.76E−11
2006-07-21	SJ9160	feii	10.701	5.61E−11
2006-07-21	SJ9160	pabeta	10.941	1.11E−10
2006-07-21	HD161903	hcont	7.055	1.94E−9
2006-07-21	HD161903	Ms	6.985	3.59E−11
2008-05-11	HD201941	pabeta	6.70	5.38E−09
2008-05-11	HD201941	hcont	6.64	2.85E−09
2008-05-11	HD201941	feii	6.64	2.36E−09
2008-05-11	HD201941	jcont	6.70	6.80E−09
2008-05-11	HD201941	Ms	6.60	5.11E−11

almost the maximum distance, the angular resolution was degraded substantially by the anisoplanatic effect (see, e.g., de Pater et al., 2004). As a result, the wide camera images fully sampled the PSF, and no advantage in angular resolution would be achieved by using the narrow camera. At 5 μm the background intensity is so high that observations at this wavelength can only be performed with the narrow camera.

All images were processed using standard near-infrared data reduction techniques (flat-fielded, sky-subtracted, with bad pixels replaced by the median of surrounding – typically 8 – pixels). The geometric distortion in the images was corrected using the "dewarp" routines provided by Brian Cameron of the California Institute of Technology.[1] The absolute calibration of the images was set by a combination of: (i) observations of the IR standard stars HD161903 and SJ9160 in 2006 and HD201941 in 2008 (Table 2; Elias et al., 1982; Persson et al., 1998); (ii) observations of Io and Europa (Section 2.3), and (iii) the disk-averaged IRTF spectrum presented in Section 3.3. We estimate our final flux calibration to be accurate to $\lesssim$15–20%. From features on Jupiter that appear to be unresolved we determined a typical resolution near the red spots of ~0.12–0.16″ (~500–600 km) in the full disk (1.2–2 μm) images, and 0.08–0.10″ at 5 μm (~400 km) (see Table 4).

2.2. HST observations

On 24 and 25 April 2006 (UT) we used HST's Advanced Camera for Surveys (ACS) with both its High Resolution Channel (HRC) and Wide Field Camera (WFC) (GO/DD 10782). On 9 and 10 May 2008 (UT) we used the Wide Field Planetary Camera 2 (WFPC2) to observe Jupiter (GO 11102). A summary of the observations is given in Table 3. We used standard HST pipeline processing to convert the data into photometric units (Pavlovsky et al., 2006). Cosmic ray strikes and geometric distortion were removed using crutil (a package within IRAF, Tody, 1993) and drizzle within PyRAF (a package from the Space Telescope Science Institute).

A typical resolution obtained with HST is usually slightly less than 2 pixels across (Table 4); indeed, for the ACS/HRC images from April 2006 we determined a resolution of 163 km near the GRS and Oval BA (Asay-Davis et al., 2009).

2.3. Image preparation for analysis

A summary of the observations with the relevant ephemeris parameters is given in Table 4. To compare images where Jupiter is observed in reflected sunlight (HST and 1.1–1.8 μm Keck) with previous results and with physical models, we converted the observed flux densities, F_J, to the dimensionless parameter I/F, where I is the reflected intensity and πF the solar flux density at Jupiter's distance (e.g., Hammel et al., 1989):

$$\frac{I}{F} = \frac{r^2}{\Omega}\frac{F_J}{F_\odot}, \tag{1}$$

with r Jupiter's heliocentric distance (in AU), $\pi F_\odot$ the Sun's flux density at Earth's orbit (taken from Colina et al. (1996)), and Ω is the solid angle (in steradians) subtended by the body or a pixel on the detector. By this definition, $I/F = 1$ for diffuse scattering from a (Lambert) surface, and is equal to the geometric albedo if the object

[1] http://www2.keck.hawaii.edu/inst/nirc2/forReDoc/post_observing/dewarp/nirc2dewarp.pro.

Table 3
HST observations.

Start date (UT) h:m	Instrument	Filter	Wavelength (μm)	T (integration)	# Frames
2006-04-24 14:58	ACS/HRC	F658N	0.658	10	4
2006-04-24 15:00	ACS/HRC	F435W	0.435	3	4
2006-04-24 15:02	ACS/HRC	F502N	0.502	10	4
2006-04-24 15:09	ACS/HRC	F892N	0.892	20	2
2006-04-24 15:11	ACS/HRC	F330W	0.336	10	2
2006-04-25 00:35	ACS/HRC	F435W	0.435	4	4
2006-04-25 00:35	ACS/HRC	F502N	0.502	10	4
2006-04-25 00:45	ACS/HRC	F658N	0.658	10	4
2008-05-09 23:18	WFPC2	F255W	0.260	100	1
2008-05-09 21:59	WFPC2	F336N	0.334	10	1
2008-05-09 21:39	WFPC2	F410N	0.410	8	4
2008-05-09 21:36	WFPC2	F502N	0.502	14	4
2008-05-09 21:31	WFPC2	F673N	0.673	4	11
2008-05-09 23:25	WFPC2	FQCH4P15	0.893	70	1
2008-05-10 09:07	WFPC2	F336N	0.334	10	1
2008-05-10 08:46	WFPC2	F410N	0.410	8	1
2008-05-10 08:43	WFPC2	F502N	0.502	14	1
2008-05-10 08:38	WFPC2	F673N	0.673	4	8
2008-05-10 08:50	WFPC2	FQCH4P15	0.893	70	1

The 2006 data were obtained under HST program GO/DD 10782; the 2008 data under GO 11102. Times indicated are the start times of the first frame in the orbit.

Table 4
Instrument and ephemeris details.

Date (UT)	Telescope/instrument	Filter	Geoc. dist. (AU)	Pixel size (″)	Pixel size (km)
2006-04-24/25	HST/ACS/HRC	F330W	4.432	0.028	90.0
2006-04-24/25	HST/ACS/HRC	F435N	4.432	0.028	90.0
2006-04-24/25	HST/ACS/HRC	F502N	4.432	0.028	90.0
2006-04-24/25	HST/ACS/HRC	F658W	4.432	0.028	90.0
2006-04-24	HST/ACS/HRC	F892N	4.431	0.028	90.0
2006-07-21	Keck/NIRC2	hcont	5.121	0.04	148.5
2006-07-21	Keck/NIRC2	feii	5.121	0.04	148.5
2006-07-21	Keck/NIRC2	pabeta	5.121	0.04	148.5
2006-07-21	Keck/NIRC2	Ms	5.121	0.01	36.9
2008-05-09/10	HST/WFPC2	F673N	4.661	0.046	155.5
2008-05-09/10	HST/WFPC2	F502N	4.661	0.046	155.5
2008-05-09/10	HST/WFPC2	F410N	4.661	0.046	155.5
2008-05-09/10	HST/WFPC2	F255N	4.661	0.046	155.5
2008-05-09/10	HST/WFPC2	FQCH4P15	4.661	0.046	155.5
2008-05-11	Keck/NIRC2	pabeta	4.635	0.04	134.5
2008-05-11	Keck/NIRC2	hcont	4.635	0.04	134.5
2008-05-11	Keck/NIRC2	feii	4.635	0.04	134.5
2008-05-11	Keck/NIRC2	jcont	4.635	0.04	134.5
2008-05-11	Keck/NIRC2	Ms	4.635	0.01	33.4

A typical resolution of the Keck 1–2 μm observations is 0.12–0.16″ and 0.08–0.10″ at 5 μm. A typical resolution of the HST observations is slightly less than 2 pixels.

is observed at normal incidence and a solar phase angle of 0°. While the HST data are well calibrated photometrically, photometry can be problematic for ground-based measurements due to, e.g., atmospheric fluctuations. As a check on the final photometry of our Keck observations, we list the disk-averaged I/F of the satellites Io and Europa (if visible in the images) in Table 1; these values agree with other published values (e.g., Spencer et al., 2004).

The units on the 5-μm images were converted to brightness temperature using the Planck equation and the assumption of a blackbody radiator.

Since Jupiter rotates quickly, features on the planet will shift from image to image, even if taken only minutes apart. This complicates mosaicing images together, a process that is in particular essential to stitch the small (field of view) 5-μm images together to view a large fraction of Jupiter's disk. To facilitate this process, we deprojected all processed images onto a latitude–longitude grid, and aligned a synthetic Jupiter image against the real Jupiter data (Asay-Davis et al., 2009; Lii et al., 2010). To deproject successfully, at least part of Jupiter's limb needs to visible on the image. If no limb is visible in the data, we match cloud features to other images where the limb can be fitted.

3. Results: I. Jupiter in reflected sunlight

3.1. Images

Final processed Keck images at 1.1–1.8 μm from 21 July 2006 and 11 May 2008 are shown in Figs. 2 and 3, respectively. In the upper right corner of each figure the satellite used for wavefront sensing is visible (Io or Europa, Table 1).

Figs. 4 and 5 show HST views of an area on Jupiter that includes the GRS and Red Oval BA, after deprojection onto a rectangular grid. In all Figs. 2–5 the GRS and Oval BA show up prominently. In July 2006 the two ovals were passing each other, as they do every other year. In May 2008 a third, relatively small, red spot (referred to as Oval 2 by Rogers and Mettig (2008)) was discovered to the west of, and in the same latitude band as, the GRS. This spot was later observed to pass in between the GRS and Oval BA, being shredded in the process (Sanchez-Lavega et al., 2008). At 1.65 μm (Fig. 3) there is a small bright spot just east of the GRS, where streamlines appear to come together.

The three red spots have much in common: (i) They typically consist of a 'core' surrounded by a 'ring'. (ii) Relative to the back-

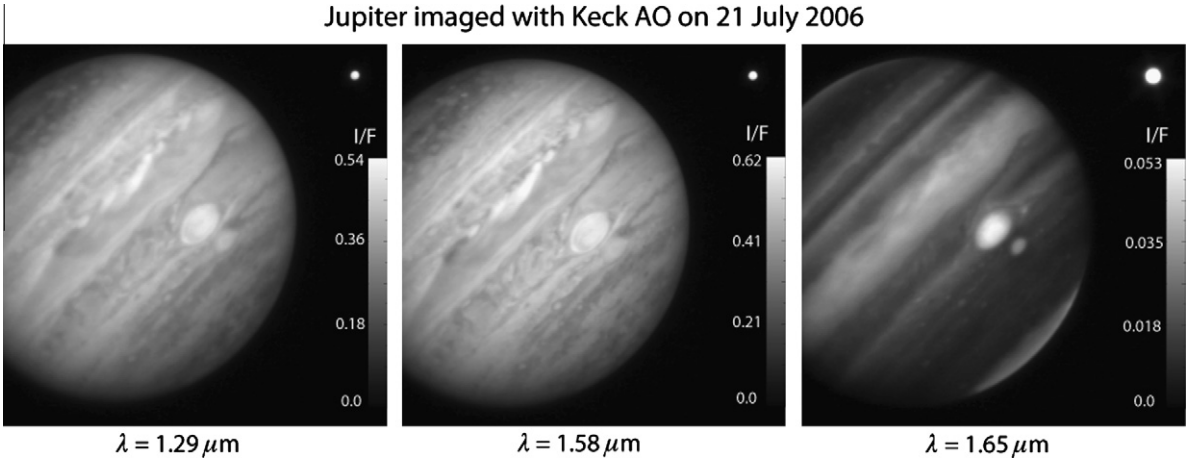

Fig. 2. Keck AO images from UT 21 July 2006, at 1.29, 1.58 and 1.65 μm. The (linear) intensity scale in each image is stretched so the contrast is optimal. Io is visible in the upper right corner.

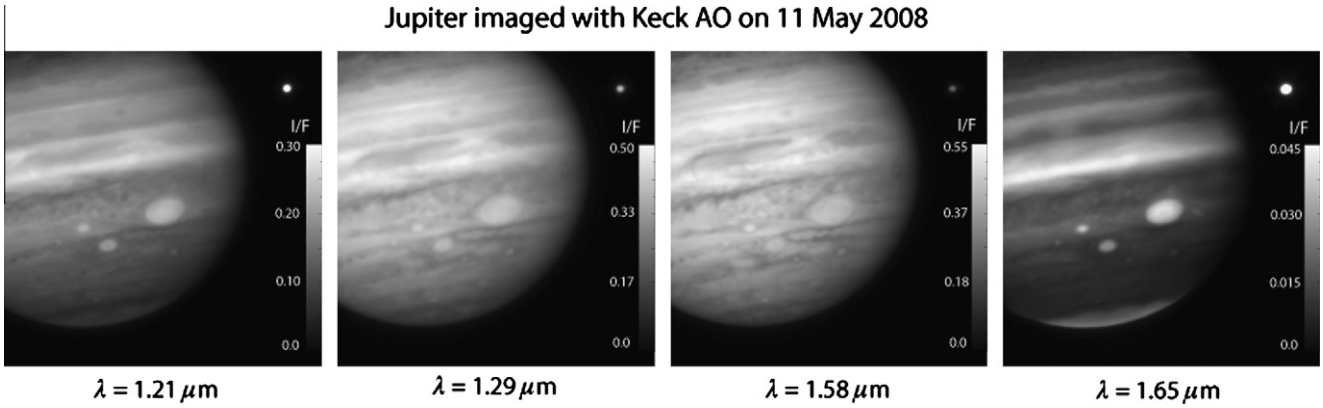

Fig. 3. Keck AO images from UT 11 May 2008, at 1.21, 1.29, 1.58 and 1.65 μm. The (linear) intensity scale in each image is stretched so the contrast is optimal. Europa is visible in the upper right corner.

ground, they are dark at UV wavelengths, and (iii) bright in the near-infrared. Their relative brightness is largest at wavelengths where methane gas is absorbing most strongly, which suggests that all three ovals rise well above their surroundings. UV absorption by high altitude haze may explain why the ovals are dark at these short wavelengths. The variation in each oval's reflectivity with wavelength can be used to derive the vertical structure of each vortex (Section 3.3).

Despite the above similarities, there are also pronounced differences in spot morphology and color. In color-composite images (Fig. 11c; see also Fig. 1c of Cheng et al. (2008)) it is only the ring in Oval BA that is red, while both the ring and core of the GRS are red, with the core being reddest. The small (short-lived)red spot discovered in 2008 is as red as the GRS. The differences in the ovals' colors may be explained by the differences in their reflectivities at UV/blue wavelengths (Figs. 4 and 5), where the GRS shows most absorption (i.e., is darkest) in the core, while for Oval BA the core is more reflective (brighter) than the ring around the core. Similar differences can be seen in Fig. 2 of Cheng et al. (2008). To emphasize differences between the GRS and Oval BA that pertain to their red color, we created "chromophore" maps (Fig. 6) by subtracting and normalizing a red and UV/blue HST image: $[(F658N - F435N)/F658N]$. The red filter is sensitive to clouds, and did not show any changes in Oval BA's reflectivity when its color changed. In contrast, large changes were observed at 435 nm, between a before (January 2005) and after (April 2006) image (Simon-Miller et al., 2006; Pérez-Hoyos et al., 2009). The reflectivity at this wavelength is strongly affected by aerosols above Jupiter's main cloud deck. We normalize the color difference image by the red reflectivity in order to remove the effect of a spatially-variable cloud opacity. Superposed in Fig. 6 are approximate contours (the dotted lines) that outline the location of the peak values in the local wind velocity field, as determined by Asay-Davis et al. (2009). The visible clouds are not aligned with any dynamical features of the vortices, and the areas covered by the clouds extend well beyond these maximum wind velocity contours. In contrast to the clouds, both the haze and chromophores over Oval BA are almost entirely confined within the ring of maximum azimuthal velocity, but in the GRS both haze and chromophores spill out beyond the ring of maximum velocity. The reason for this difference is not clear, but may be related to the more complex circulation in the GRS, with its inner region of almost zero vorticity (Shetty and Marcus, 2010). Within the GRS, the coloration of the chromophores is most intense in this inner region and in the clouds just exterior to the ring of maximum velocity, whereas Oval BA's chromophores are concentrated in an annulus just interior to this ring.

3.2. I/F measurements

On each deprojected image, we determined the I/F of the GRS, Oval BA, and (in 2008) the small red Oval 2. In 2008 we also determined the I/F at the equator near the center of the disk and of the

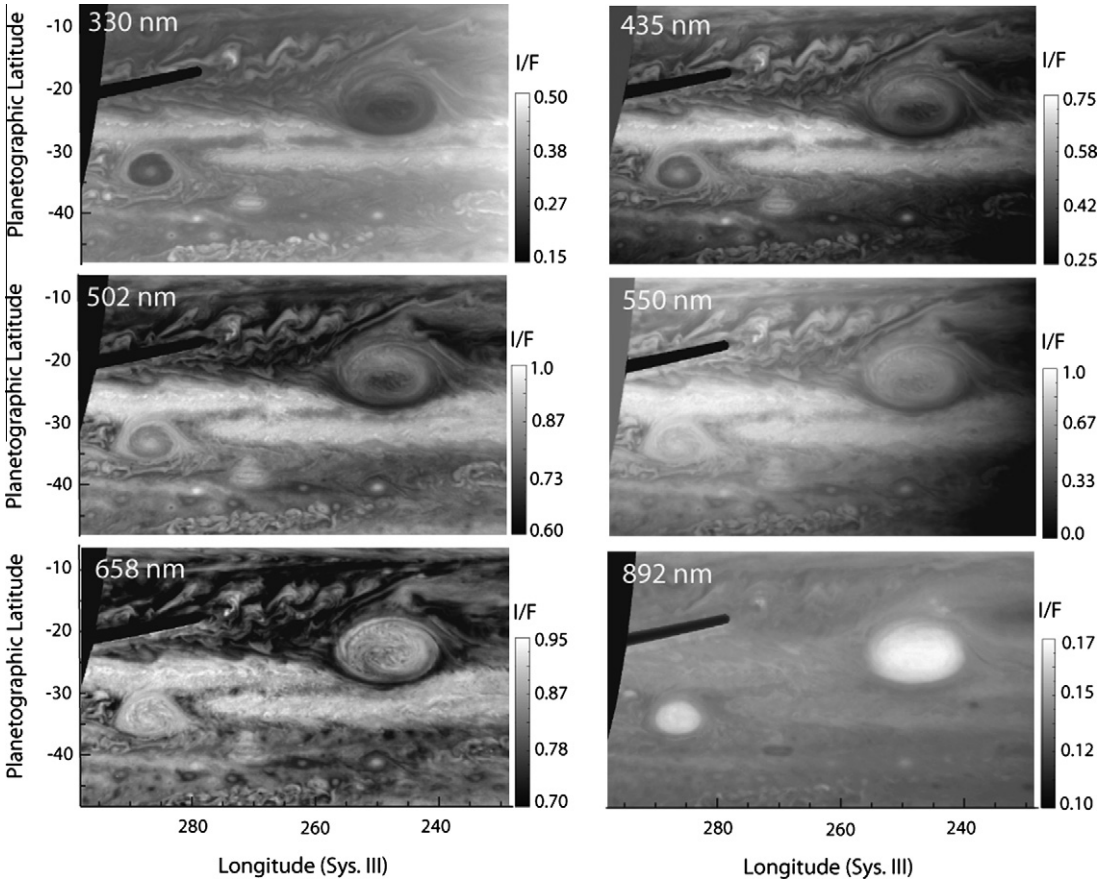

Fig. 4. HST images at different wavelengths (330–892 nm) of the GRS and Red Oval BA, after deprojection onto a rectangular grid. These images were taken with the ACS/HRC on UT 24 April 2006. Limbdarkening was 'corrected' by applying a Minnaert correction with $k = 1.0$; the resulting I/F values are shown on the right side of each frame. The black stripe on the left side in each image is the occulting finger of the detector.

two white Ovals A5 and A6 just south of the GRS (Fig. 5; this nomenclature is consistent with Rogers and Mettig (2008)). For the GRS we determined the median value at the center in a $3^\circ \times 3^\circ$ square box. For the ovals we used a $0.6^\circ \times 0.6^\circ$ square box at the center, and for Oval BA we also placed one such small box on its red ring, to the west of the center. At the equator we used a small rectangular box, 2° in the zonal direction and 1° along the meridian.

In order to compare the I/Fs for the different features between wavelengths and at different times, we used a Minnaert function to correct for variations caused by viewing angle and illumination effects:

$$I(\mu, \mu_0) = I_0 \mu_0^k \mu^{k-1}, \quad (2)$$

with μ the cosine of the emission angle (angle between the line of sight and normal to the surface) and μ_0 the cosine of the incidence angle (angle a solar ray makes with the normal to the surface). Usually the Minnaert coefficient $k \approx 0.9$–1.0; for features at wavelengths where we had more than one observation, we determined k from a fit to the data of the feature of interest. The Minnaert coefficients and derived I_0/F values are tabulated in Table 5. In Table 6 we summarize the range in μ and μ_0 for the data used to fit k. Fig. 7 shows the I_0/F values for 2008 graphically. As also seen in Figs. 4 and 5, but quantified in Fig. 7, the GRS, Oval 2, and the red ring of Oval BA have relatively low reflectivities at UV–blue wavelengths, while at 673 nm all spots have high reflectivities ($\sim$0.85–0.9). Hence the visibly red color must indeed be attributed to the low reflectivity at UV–blue wavelengths. In addition, the differences between the spectra explain the different colors red between these three ovals. At 893 nm the reflectivites of all spots are about a factor of 10 lower than at visible wavelengths. This wavelength coincides with a methane absorption band, and hence most sunlight at this wavelength is absorbed by methane gas in Jupiter's atmosphere, and only material at high enough altitudes reflect radiation. The GRS, which has the lowest reflectivity at UV–visible wavelengths, is the brightest feature on the disk at near-IR wavelengths. In the strong 1.65-μm methane absorption band, all three red spots are much brighter than their environment and the white ovals.

Fig. 8 shows the I_0/F of the GRS and Oval BA in 2006 (dots), compared to the 2008 data at the same wavelengths next to it (squares; the 2006 values are shifted to the left by 40 nm). The reflectivity of the GRS remained remarkably stable at 330–500 nm. In contrast, both the center and red ring of Oval BA brightened by $\sim$10%, which is more than could be explained by possible uncertainties in the Minnaert coefficient; hence this relative brightening is real. At near-infrared wavelengths the reflectivities of both the GRS and Oval BA may have decreased somewhat between 2006 and 2008; however, given the 10–20% absolute uncertainties in these data, we do not claim this variability to be real.

3.3. Radiative transfer (RT) model

To determine the vertical structure and altitude of the vortices, we used a radiative transfer (RT) code at near-IR wavelengths that was originally developed for Titan (Ádámkovics et al., 2007), and adapted to the giant planets by Luszcz-Cook et al. (2010). We adopt a temperature-pressure profile for Jupiter's atmosphere as derived from the Galileo Probe data (Seiff et al., 1998), and calculate the

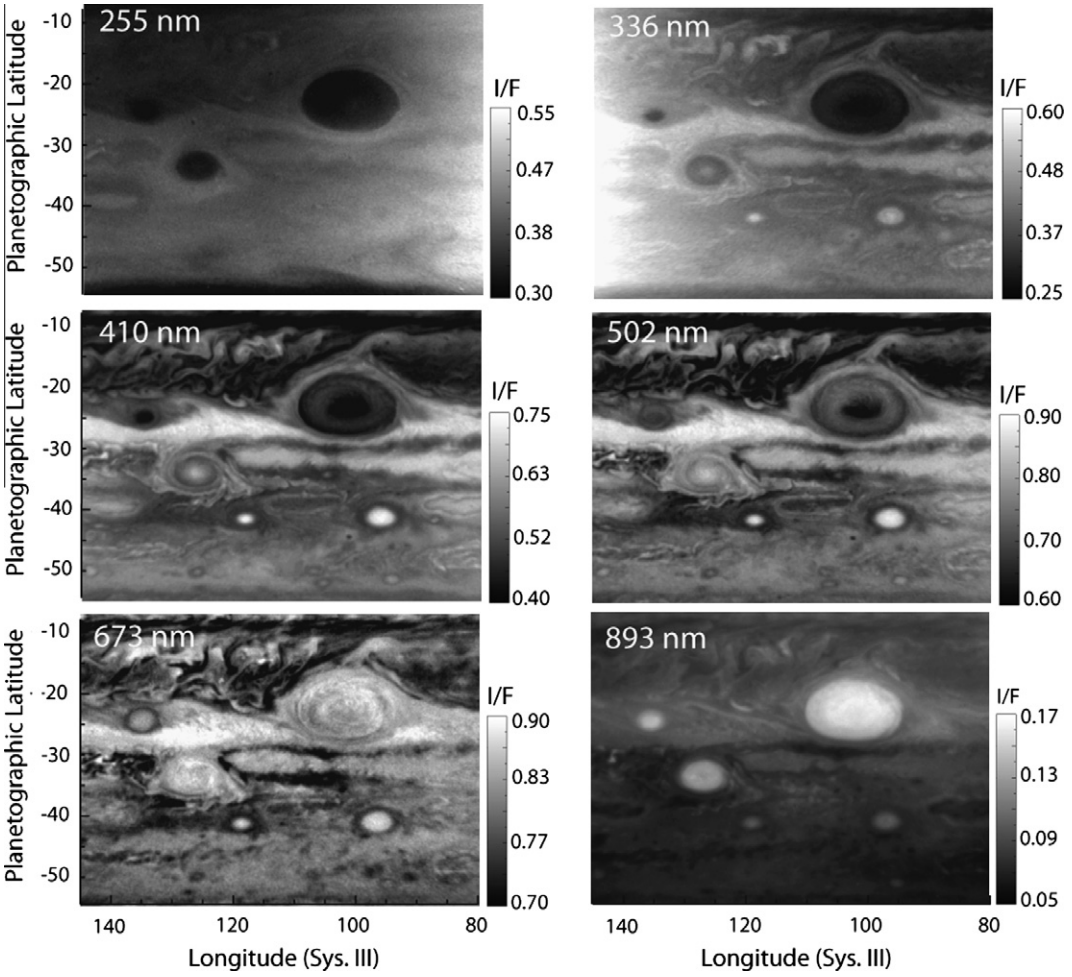

Fig. 5. HST images of the GRS, Red Oval BA, red Oval 2, and the two white Ovals A5 and A6, after deprojection onto a rectangular grid (see Fig. 4). These images were taken with the WFPC2 on UT 9 May 2008.

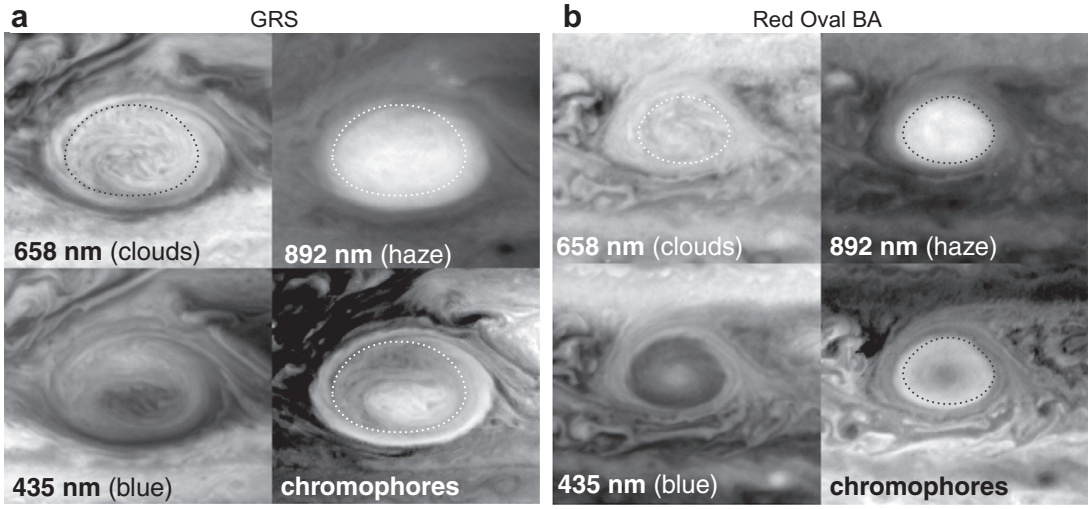

Fig. 6. Detailed views of (a) the GRS and (b) Oval BA at different wavelengths, as indicated, from images taken on UT 24 April 2006 (from Fig. 4). The "chromophore" maps were constructed from the red and blue images: $[(F658N - F435N)/F658N]$. Superposed are approximate contours (the dotted lines) that outline the location of the peak values in the local wind velocity field, as determined by Asay-Davis et al. (2009).

total atmospheric opacity as provided by aerosols, cloud particles, and the gases hydrogen, methane and ammonia. Absorption by hydrogen gas (collision-induced H_2–H_2, H_2–He) is calculated using the routines from Borysow (1991, 1988), for a H_2 ortho/para ratio equal to the equilibrium value. The *k*-distribution coefficients of Irwin et al. (2006) are used to calculate absorption by hydrogen-

Table 5
I_0/F[a] and k[b] for the GRS, Red Ovals BA and 2, the equator, and white Ovals A5 and A6.

Wavelength (nm)	Minnaert coefficients k	I_0/F GRS	I_0/F BA ctr	I_0/F BA ring	I_0/F Oval 2	I_0/F equator	I_0/F Oval A6	I_0/F Oval A5
HST April 2006								
330.0	0.65[d]	0.244 ± 0.003	0.323 ± 0.003	0.278 ± 0.003				
502.0	1.0	0.61 ± 0.01	0.77 ± 0.01	0.72 ± 0.01				
658.0	1.0	0.745 ± 0.005	0.792 ± 0.007	0.773 ± 0.007				
892.0	1.0[e]	0.110 ± 0.005	0.097 ± 0.005	0.095 ± 0.005				
Keck July 2006								
1290	0.9 ± 0.1	0.53 ± 0.01	0.47 ± 0.02	0.49 ± 0.02				
1580	0.9 ± 0.1	0.62 ± 0.02	0.57 ± 0.02	0.58 ± 0.02				
1646	0.9 ± 0.1	0.05 ± 0.01	0.04 ± 0.01					
HST May 2008								
255.0	0.8 ± 0.2[f]	0.29 ± 0.03	0.31 ± 0.02	0.30 ± 0.02	0.29 ± 0.02	0.26 ± 0.03	0.38 ± 0.07	
336.0	0.65[d]	0.240 ± 0.004	0.365 ± 0.005	0.307 ± 0.005	0.250 ± 0.004	0.33 ± 0.01	0.47 ± 0.01	0.50 ± 0.05
410.0	1.0	0.387 ± 0.004	0.65 ± 0.01	0.54 ± 0.01	0.45 ± 0.01	0.60 ± 0.02	0.75 ± 0.01	0.75 ± 0.1
502.0	1.0	0.62 ± 0.01	0.84 ± 0.02	0.78 ± 0.02	0.73 ± 0.01	0.80 ± 0.02	0.89 ± 0.01	0.8 ± 0.1
673.0	1.0	0.85 ± 0.01	0.87 ± 0.02	0.85 ± 0.02	0.91 ± 0.02	0.86 ± 0.02	0.90 ± 0.01	0.9 ± 0.1
893.0[c]	1.0[e]	0.095 ± 0.006	0.073 ± 0.006	0.075 ± 0.006	0.089 ± 0.006	0.13 ± 0.01	0.095 ± 0.01	0.10 ± 0.05
Keck May 2008								
1213	0.9 ± 0.1	0.30 ± 0.02	0.22 ± 0.01	0.23 ± 0.01	0.24 ± 0.02	0.26 ± 0.02	0.18 ± 0.01	0.16 ± 0.01
1290	0.9 ± 0.1	0.52 ± 0.02	0.44 ± 0.02	0.45 ± 0.02	0.46 ± 0.02	0.47 ± 0.02	0.41 ± 0.01	0.36 ± 0.01
1580	0.9 ± 0.1	0.56 ± 0.02	0.49 ± 0.02		0.53 ± 0.02	0.51 ± 0.02	0.47 ± 0.01	0.43 ± 0.01
1646	0.9 ± 0.1	0.05 ± 0.01	0.03 ± 0.01		0.04 ± 0.01	0.04 ± 0.01	0.016 ± 0.005	0.014 ± 0.005

[a] I_0/F: the observed I/F has been corrected for viewing angle and illumination effects, using the Minnaert coefficient k in Eq. (2). Uncertainties in I_0/F include the uncertainty in k (where given), but do not include the absolute photometric uncertainty (10–20% for the Keck data, Section 2.1).
[b] Minnaert coefficient k from Eq. (2). For the Keck data, $k = 0.9 \pm 0.1$ was adopted based upon a fit to zonal bands with a similar brightness.
[c] Corrected for "blue leak" (Lii et al., 2010).
[d] k at 330 nm was assumed to be equal to that at 336 nm. k varies from feature to feature: $k = 0.75$ for center Oval BA; $k = 0.70$ for Oval BA's (red) ring; $k = 0.9$ for the white ovals.
[e] $k = 1.0$ adopted from Wong et al. (2010).
[f] Assumed range of Minnaert coefficients.

broadened methane, and absorption by ammonia gas is determined with the parameters and algorithm as described by Bowles et al. (2008). The helium abundance (mole fraction) is set to 0.136, and for methane we adopt a constant value of 2.0×10^{-3} (Wong et al., 2004). Throughout our region of interest, the NH_3 abundance is set equal to 7×10^{-5}, and follows the saturated vapor pressure curve as appropriate (de Pater et al., 2005). Aerosols are currently treated as Mie scatterers, with an effective particle radius, r_p, and index of refraction, m_r and m_i. Rayleigh scattering is calculated according to the algorithm of Hansen and Travis (1974). Optically thick clouds are modeled as perfect reflectors with an asymmetry parameter of 0.5. We divide the atmosphere in 120 layers, distributed logarithmically between .28 mbar and 4.1 bar. The RT equations are then solved using a two stream approximation.

Banfield et al. (1998) and Munoz et al. (1999) performed detailed RT calculations of several features in Jupiter's atmosphere; Pérez-Hoyos et al. (2009) modeled Oval BA. All these authors modeled observations at wavelengths below 1 μm. We use these previous results as a starting point to model our Keck AO data at 1–2 μm. As in the previous models, we adopt an index of refraction that is representative of NH_3–ice (Martonchik et al., 1984): we effectively set m_i to zero ($m_i = 1.0 \times 10^{-4}$), and adopt $m_r = 1.43$. The optical depths of the NH_3–ice (at ~0.7–0.75 bar) and NH_4SH (at ~2.5 bar) clouds were set at 10 and 30, respectively (large values, as in Banfield et al. (1998); the lower cloud has no effect on the calculations); the location of these clouds follows from thermochemical equilibrium calculations (see, e.g., de Pater et al., 2001, 2005).

To check our model we first compare it to a 'disk-averaged' spectrum of Jupiter. We retrieved this spectrum from the NASA Infrared Telescope Facility (IRTF) Spectral Library; it was taken with the SpeX instrument on the IRTF on Mauna Kea (Rayner et al., 2009). Since the spectrum was taken through a 15″ long slit, much smaller than Jupiter itself, we scaled the spectrum to a disk-averaged spectrum of the planet taken by Karkoschka (1994) at wavelengths $\lesssim 1$ μm; the two spectra overlap between 0.8 and 1 μm. The scaled IRTF spectrum is shown in Fig. 9. To check the absolute calibration of the IRTF spectrum, we compared it to a low (spectral) resolution whole-disk Cassini VIMS spectrum, taken during Cassini's encounter with Jupiter in 2000 (K. Baines, private communication); the two spectra match very well.

We choose not to vary the CH_4 and NH_3 profiles in our model atmosphere, as these are measured quite reliably. Moreover, as we primarily probe layers in the atmosphere above the NH_3–ice cloud, the gaseous ammonia abundance follows the saturated vapor curve, and hence is not very sensitive to the precise value below the NH_3–ice cloud. Admittedly, we ignore potential effects due to photochemistry; however, we do not think this will affect the results in any significant way. As modelers before us, we leave m_r and m_i fixed at the NH_3–ice values, as discussed above. Only in extreme circumstances, such as after an impact (de Pater et al., 2010), may m_i be increased so much (a factor of ~100) as to affect the modeled I/F. This limits our choice of free parameters to the aerosols, with r_p, n or τ_h, and the thickness and altitude of the haze layers above the NH_3–ice cloud, itself being located at 0.70–0.75 bar. The geometric optical depth of the haze in a layer of our model atmosphere is defined:

$$\tau_h \equiv nZ\pi r_p^2, \tag{3}$$

with Z the thickness of the layer (in cm), n the particle number density (cm^{-3}), and πr_p^2 the surface area (cm^2) subtended by a particle. The wavelength-dependent opacity, τ, due to the haze particles is determined at each level in the atmosphere. Numerous models were run, with different values for the haze parameters (r_p, n or τ_h), and the thickness, location and number (1–4) of the haze layers. A good fit to the IRTF spectrum is obtained with values for r_p, n and τ_h in three different haze layers above the NH_3–ice cloud: layer 1 at 2–200 mbar, layer 2 at 200–650 mbar and layer 3 at 650–700 mbar. These values are summarized in Fig. 10a. The model spectrum is

Table 6
Range in μ and μ_0 for calculations of Minnaert coefficients in Table 5.

Wavelength (nm)	GRS, μ	GRS, μ_0	BA, μ	BA, μ_0	Oval 2, μ	Oval 2, μ_0	Oval 6, μ	Oval 6, μ_0	Oval 5, μ	Oval 5, μ_0
HST April 2006										
502.0	0.987	0.864–0.653	0.988	0.858–0.836						
658.0	0.987	0.865–0.626	0.988	0.853–0.838						
HST May 2008										
336.0	0.854–0.878	0.909–0.814	0.852–0.672	0.852–0.672	0.845–0.540	0.854–0.649	0.735–0.702	0.772–0.641	0.735–0.702	0.772–0.641
410.0	0.887–0.863	0.926–0.793	0.848–0.718	0.849–0.624	0.846–0.598	0.852–0.697	0.693–0.756	0.629–0.722	0.693–0.756	0.629–0.722
502.0	0.747–0.873	0.835–0.807	0.850–0.703	0.846–0.606	0.842–0.580	0.853–0.682	0.748–0.763	0.777–0.734	0.777–0.734	0.777–0.734
673.0	0.902–0.856	0.934–0.782	0.854–0.383	0.842–0.502	0.854–0.538	0.854–0.423	0.762–0.768	0.780–0.745	0.762–0.768	0.780–0.745

The number of images used for each feature varies from 2 to 7; for most features there were three or four images.

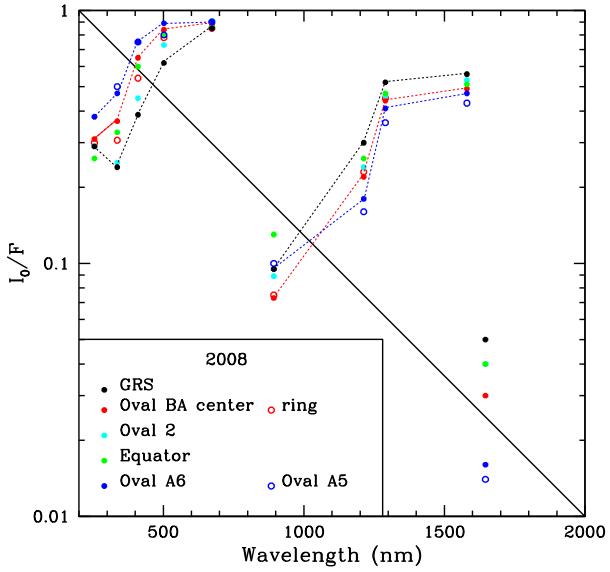

Fig. 7. I_0/F values (Eq. (1)) as a function of wavelength for various features on Jupiter's disk, as observed with HST and Keck in May 2008. To help guide the eye, we connected a few of the symbols for the GRS, Oval BA, and Oval 6 by dashed lines. Errorbars are not plotted to avoid too much cluttering; see Table 5 for individual values. (The web version of this article contains color.)

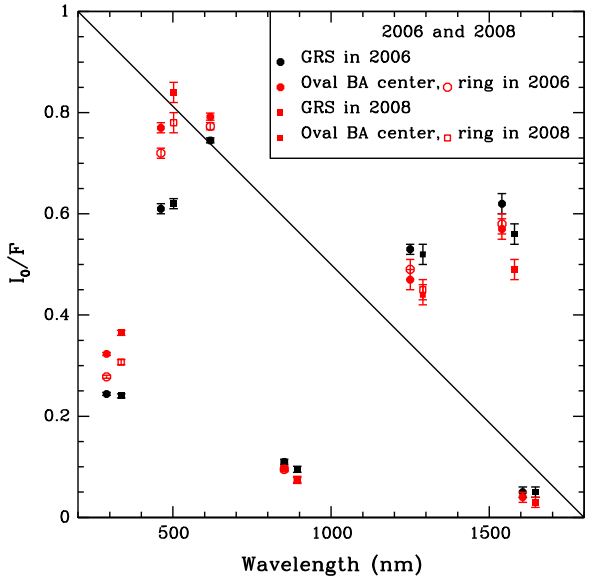

Fig. 8. I_0/F values as a function of wavelength of the GRS and Oval BA, as observed with HST and Keck in 2006 (circles; shifted to the left by 40 nm). For comparison we plotted the 2008 data (squares) at the same wavelengths next to it (squares; note that there are no 2008 data at 658 nm). Note the change in *y*-axis from logarithmic in Fig. 7 to linear in this figure. In this figure, we did include errorbars; for the Keck data we did not include the photometric uncertainties in the measurement errors (see Table 5). At some wavelengths (892, 1580, 1646 nm) Oval BA's red ring is essentially indistinguishable from its center. (The web version of this article contains color.)

superposed on the IRTF spectrum in Fig. 9; we show Earth's transmission spectrum at the top of the figure to help judge the accuracy of the IRTF spectrum at different wavelengths. Normalized contribution functions in the near-IR filters of our Keck observations (Table 1) for this IRTF model are shown in Fig. 11 (for the methodology, see Ádámkovics et al., 2006). The contribution functions show that we are most sensitive to the stratosphere at 1.65 μm and least at 1.58 μm; at 1.58 μm most opacity is provided by the haze just above the NH_3–ice cloud.

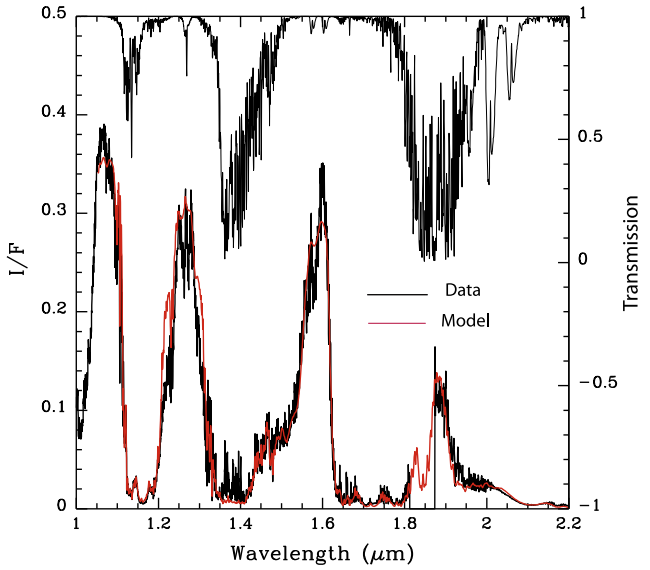

Fig. 9. Disk-averaged spectrum of Jupiter from Rayner et al. (2009), retrieved from the IRTF Spectral Library, and scaled as described in the text. Superposed is a model that matches the spectrum very well (see Fig. 10a). A transmission spectrum of Earth's atmosphere is shown at the top. (The web version of this article contains color.)

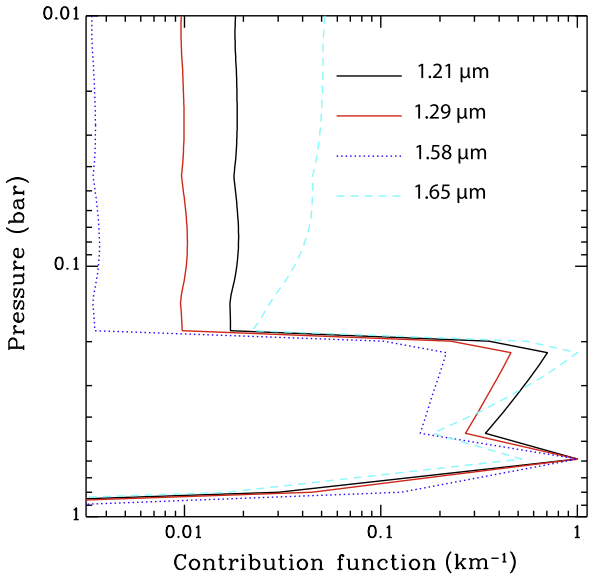

Fig. 11. Normalized contribution functions at near-IR wavelengths for the model that matches the IRTF SpeX spectrum shown in Fig. 9. Contribution functions were calculated according to the algorithm of Ádámkovics et al. (2006). (The web version of this article contains color.)

As shown in Fig. 9, our model spectrum matches the IRTF spectrum everywhere, except at ~1.22 μm and 1.30 μm, where the modeled brightness is a factor of ~1.3–1.4 higher than the observations. Changing the haze parameters such as to fit these regions, result in large discrepancies at the ~1.5-μm and ~2-μm wavelength ranges. Similarly, changing the NH_3 abundance below the clouds, and/or away from the saturated vapor curve above the clouds, cannot solve the dilemma. Since the 1.22-μm wavelength region corresponds exactly to the narrowband jcont filter on the Keck telescope used to image Jupiter (Table 1), we investigated this discrepancy in some detail: Bowles et al. (2008) show that the NH_3 absorption lines near 1.22 and 1.30 μm are weaker than the optically thick lines near 1.5 and 2 μm. As it is harder to get precise measurements for weaker transitions, the measurement accuracy at 1.22 and 1.30 μm is probably lower. Indeed, when comparing transmission models to the measured ammonia spectrum, Bowles et al. (2008) show an rms error at these wavelengths that are two times larger than those found for the much stronger lines near 1.5 and 2 μm. The authors further point out that the measurements were made between 210 and 290 K; in particular extrapolation to lower temperatures may not be quite accurate. Based on this information, we conclude that the discrepancy between model and data near 1.22 and 1.30 μm must be caused by inaccuracies in the laboratory data of the NH_3 absorption spectrum at these wavelengths, and we multiply our model fits in the jcont filter by a factor ~0.75.

Although the model fits the spectrum extremely well, we should note that there is some degeneracy between particle size and density; however, it is beyond the scope of this paper to explore the full parameter space, which is best done by fitting spectra

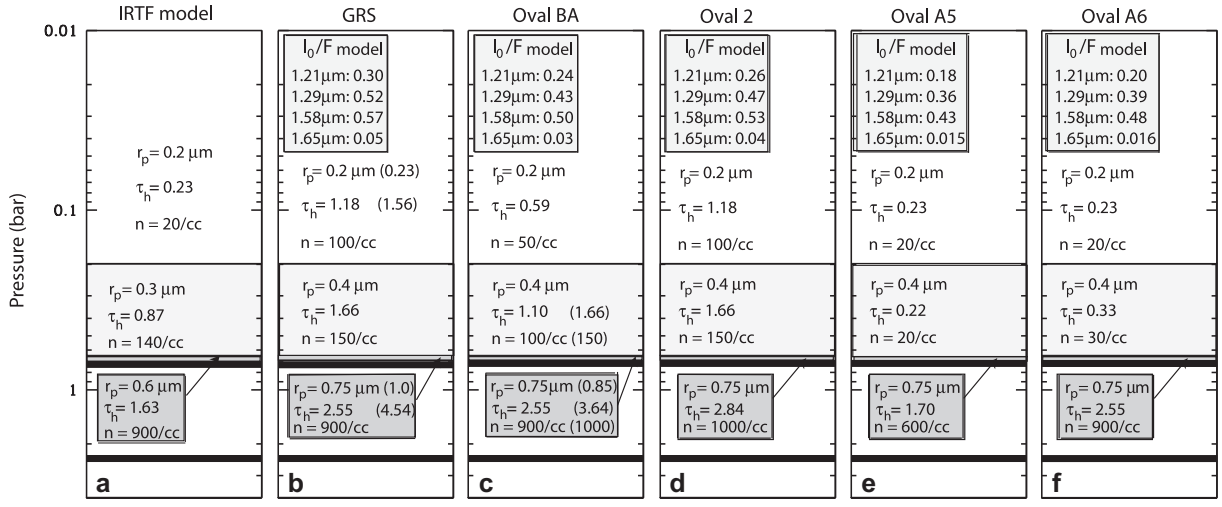

Fig. 10. (a) Model that matches the IRTF spectrum shown in Fig. 9. The particle number density is indicated by n, τ_h is the geometric optical depth (Eq. (3)), and r_p the particle radius. (b)–(f) Sketch of parameters that agree with the I_0/F measurements of the GRS, Oval BA and Ovals 2, A5 and A6 in 2008, respectively. The modeled values for I_0/F are indicated in the box at the top for each oval. For the GRS and Oval BA we indicated the values for parameters that need to be changed to fit the 2006 data in brackets; the largest changes are the particle size in the bottom haze layer from 0.75 μm to 1.0 μm for the GRS and to 0.85 μm for Oval BA. Also the number density for BA is 1.5 times larger in the tropospheric haze layer (200–650 mbar) in 2006. In all panels, the stratospheric haze extends up to 2 mbar. The thick black bars near 0.75 and 2.5 bar represent the NH_3–ice and NH_4SH clouds.

and limb darkening curves at wavelengths between ~0.2 and 2.5 μm simultaneously.

3.4. I_0/F model fits to the Keck data

For all five vortices and the equator at 1.2–2.4 μm, the I_0/F values (Table 5) are highest at 1.58 μm. They are roughly a factor of 2 lower at 1.21 μm, and a factor of >10 lower at 1.65 μm. We fit the particle size and density for these vortices in the same three layers as used in the IRTF model. The results are shown in Fig. 10, panels b–f. In addition to our free parameters, we list the modeled I_0/F values for each vortex. We note that, although we give values for I_0/F, the calculations were performed at the appropriate emission angles for the various ovals, and then converted to the corresponding I_0/F value for comparison with Table 5. All model results at 1.21 μm were multiplied by a factor 0.75 to correct for the ammonia absorption mismatch (Section 3.3).

All vortices can be matched with the same vertical structure (three layers) and particle sizes; we only need to change the density (or τ_h) to match the I_0/F of each individual vortex. The GRS and Oval 2 are similar in vertical structure; the differences in I_0/F are brought about by a slightly (10%) larger density in the bottom haze layer. The density in the top layer of Oval BA is about half that of the GRS; the tropospheric haze between 200 and 650 mbar in Oval BA is about two-third's that of the GRS. The main difference in the vertical structure of the white Ovals A5 and A6 is their low density in the top layers: about one-fifth's that of the GRS, i.e., essentially equal to the stratospheric haze in the IRTF model. Because the optical depth in the various haze layers of the GRS is much larger than in the IRTF and white oval models, our findings are not inconsistent with the commonly accepted view that the GRS rises up above the average cloud tops or white ovals; it is simply a matter of optical depth and radiative transfer. Although there is some degeneracy between particle size and density, our free parameters are well constrained because the different wavelengths used in our study have different contribution functions (Fig. 11). The region least constrained by our data is between ~100 and 200 mbar (see also de Pater et al., 2010).

In 2006 the I_0/F values for both the GRS and Oval BA may have been higher than in 2008. Taking the 2006 I_0/F numbers at their face value, we indicate in Fig. 10b and c the changes required to fit these data (indicated in brackets). If the changes in I_0/F are real, we find that the particle radii in 2006 must have been larger in the bottom haze layer (650–700 mbar) for both vortices: 1.0 μm in 2006 vs. 0.75 μm in 2008 for the GRS; 0.85 μm in 2006 vs. 0.75 μm in 2008 for Oval BA. The particle density for Oval BA is 50% larger in 2006 in the tropospheric haze layer between 200 and 650 mbar.

4. Results: II. 5-μm maps

At a wavelength of 5 μm one is sensitive to thermal emission from warm layers in Jupiter's deep atmosphere. As clouds block this outgoing radiation, 5-μm images reveal most clearly areas on Jupiter devoid of clouds. Images at this wavelength were first published by Westphal (1969), who showed enhanced 5-μm brightness temperatures associated with Jupiter's North Equatorial Belt (NEB). Using the Hale 5-m telescope at Palomar, Terrile et al. (1979) showed that the GRS is surrounded by a bright ring at 5 μm. Figs. 12 and 13 show mosaics from our 2006 and 2008 obser-

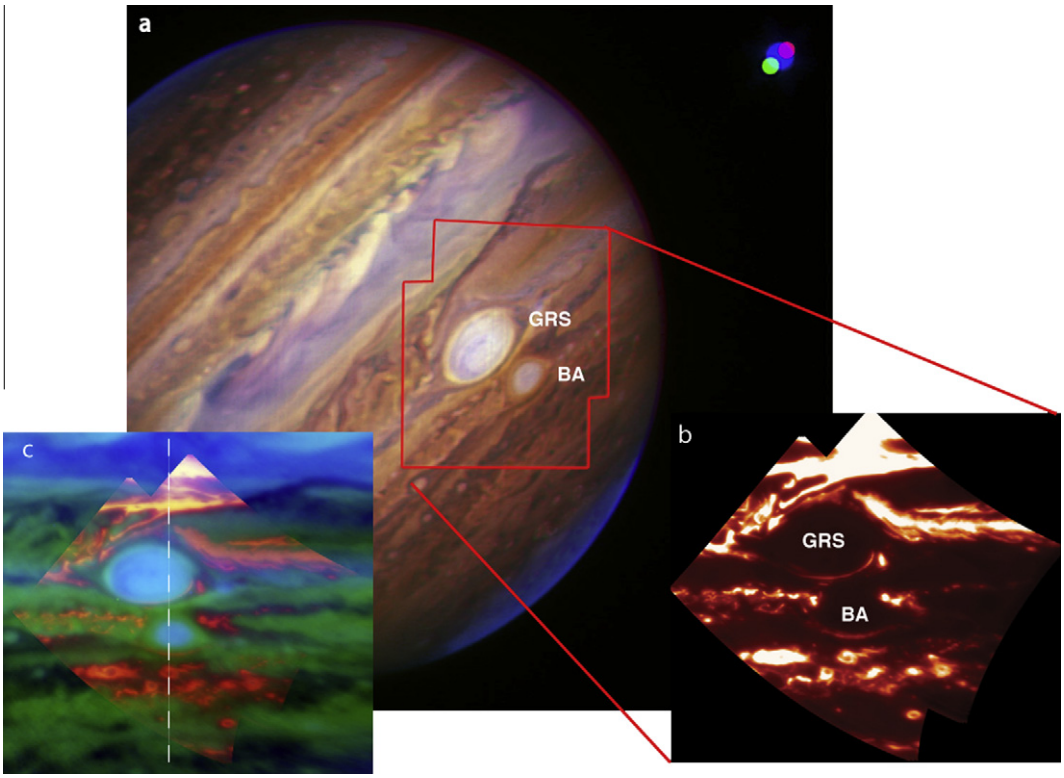

Fig. 12. (a) False-color composite Keck AO image of Jupiter in July 2006, as constructed from the images in Fig. 2. The image was sharpened using the RegiStax software, developed by Cor Berrevoets. The satellite Io is visible in the upper right corner in the green, red and blue colors of the 1.29, 1.58 and 1.65 μm filters, respectively. The motion of the satellite with respect to Jupiter during the observing sequence is clearly seen. As in Fig. 2, Io looks larger in the blue because we stretched the colors to 'brighten' Jupiter. Note that the high altitude haze above the polar hood makes the planet blue here. (b) A close-up of the two red spots through the 5-μm filter. The individual images were deprojected before mosaiced together. (c) The 5-μm image (in orange) superposed on a composite Keck image at 1.58 μm (green) and 1.65 μm (blue). Whether the 5-μm bright arc on the south side of the GRS is on the boundary of the clouds or in the dark strand below it, is hard to tell. Navigation is difficult, and the PSFs at 1.58/1.65 μm are broader than at 5 μm. The white dashed line shows the position of the scans displayed in Fig. 14.

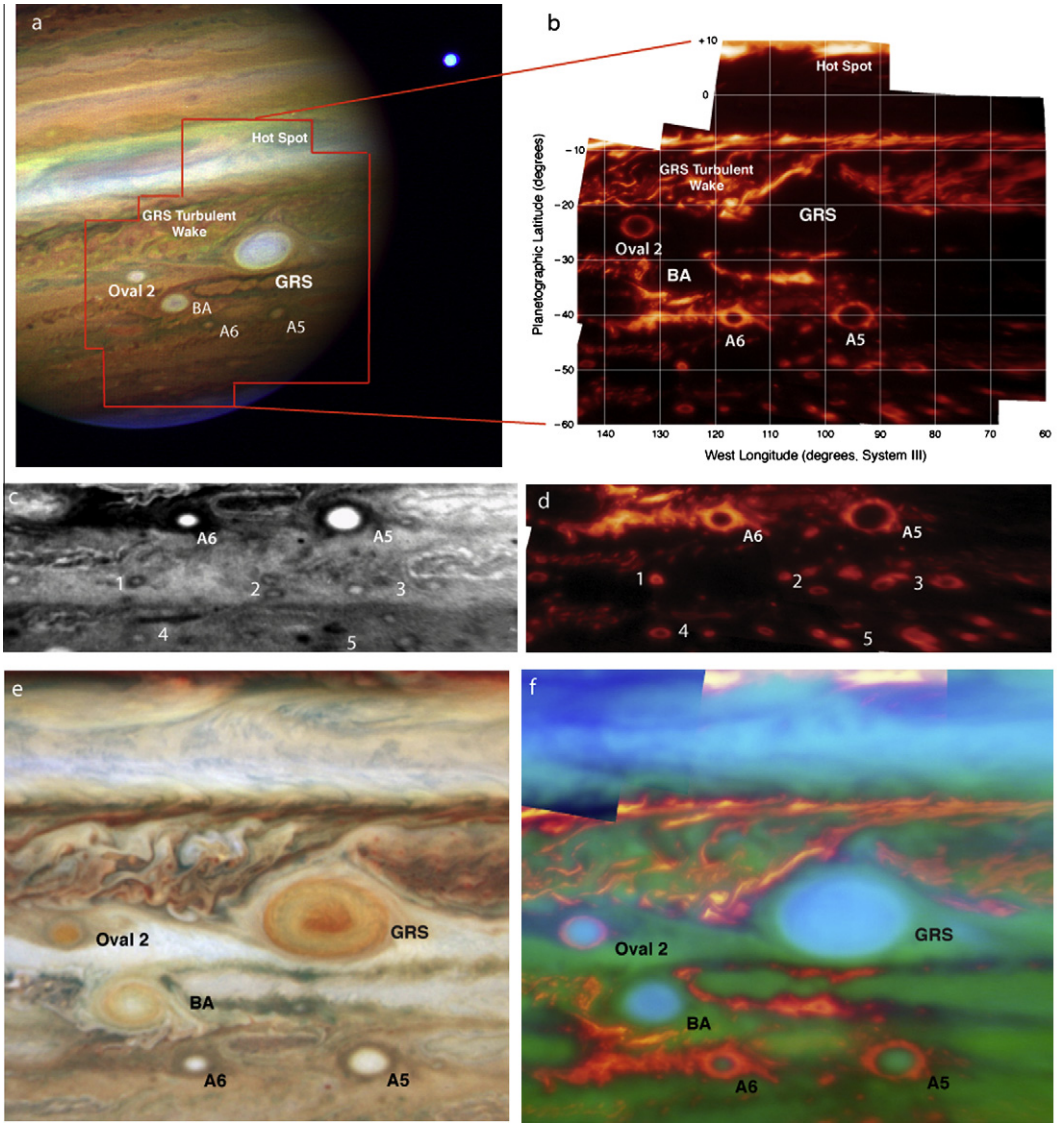

Fig. 13. (a) False-color composite Keck AO image of Jupiter in May 2008, with the satellite Europa in the upper right corner. This image is constructed from images at 1.58 (red), 1.29 (green), and 1.65 (blue) μm. The image was sharpened using the RegiStax software, developed by Cor Berrevoets. As in Fig. 12, high altitude haze above the polar hood makes the planet blue here. (b) Mosaic of the area outlined on the composite image at a wavelength of 5 μm. Individual images were deprojected before mosaiced together. (c) and (d) Detailed view of the tiny ovals south of Ovals A5 and A6. Panel (c) shows part of a 502 nm image (from Fig. 5); panel (d) shows part of panel (b). In addition to Ovals A5 and A6 we indicate five regions (1–5) to guide the reader towards ovals and features seen both at visible and 5-μm wavelengths. (e) Close-up view of the larger ovals, constructed from deprojected HST images at 673, 502 and 410 nm, using red, green and blue colors for the different filters, respectively. (f) The 5-μm image (in orange) superposed on a composite Keck image at 1.58 μm (green) and 1.65 μm (blue). Although the time between the 1.58/1.65 and 5-μm images was very short, Ovals A5 and A6 had moved slightly compared to the ovals closer to the equator.

vations at 5 μm of that portion of Jupiter's disk that contains the ovals. As these observations were obtained with the AO system on the 10-m Keck telescope at essentially the diffraction limit of the telescope, our data show the previously seen structure around the GRS in incredible detail. Clearly, the 5-μm ring around the GRS is not a simple ring.

Figs. 12 and 13 contain several panels to facilitate a comparison of differently sized ovals at different wavelengths. The 5-μm mosaic in July 2006 (Fig. 12) was confined to the GRS and Oval BA, which were passing each other during that period, as they do every 2 years. Fig. 12c shows the 5-μm mosaic superposed on a composite image constructed from data at 1.58 and 1.65 μm. As these images were taken only slightly earlier on the same night, the relative positions of the vortices had not changed much between exposures.

Six different panels from the May 2008 data are shown in Fig. 13. The 5-μm mosaic in panel (b) covers a much larger area on Jupiter than in 2006. As in Fig. 12c, we superpose this mosaic on a composite image constructed from data at 1.58 and 1.65 μm in panel (f), while panel (e) shows a color composite HST image of the same area, taken only a day earlier. All five ovals are surrounded by a ring of bright 5-μm emission, and are themselves 'cold', i.e., the center of the vortices contain clouds dense enough to block any outgoing thermal radiation. Although this is seen for all vortices, there is a difference between the two large ovals, the GRS and BA, and the smaller Ovals 2, A5, and A6. The 5-μm bright rings tightly surround the periphery of these smaller ovals, while the GRS and Oval BA are characterized by turbulent regions with areas that are bright at 5 μm. Several sharply defined emission strands are visible on the south side of the GRS and Oval BA. These strands, as well as the detailed morphology of the 5-μm emission in the turbulent areas, vary over time. Variability in 5-μm emission maps has also been seen in images at lower spatial resolutions (e.g., Fletcher et al., 2010). A comparison of the 5-μm images with

the Keck near-IR and visible light HST images (Figs. 12c, 13e and f) shows that the darker bluish-colored areas on the HST images must be cloud-free, enabling thermal 5-μm emission to escape. Such correlations between a visibly blue color and 5-μm emissions were noticed before by Ingersoll (1990), who states: "Blue regions have the highest apparent temperatures, so they must lie at the deepest levels and are only visible through holes in the upper clouds."

Further south, between ∼−45° and −60° numerous much smaller vortices can be distinguished; vortices with diameters ≲1000 km are seen as resolved features. Panels (c) and (d) in Fig. 13 highlight these vortices. In panel (c) we show an HST visible light image (502 nm), with the 5-μm mosaic covering the same area in panel (d). We indicated several (groups of) features with the numbers 1–5 to guide the eye. Note that many of the visibly dark regions are bright at 5 μm, including the large 'barge' at no. 4. At no. 3 we see two anticyclones (one on each side of the number 3), with a presumably cyclonic dark (bright at 5 μm) region in between. As Ovals 2, A5 and A6, these tiny vortices are tightly surrounded by 5-μm bright rings.

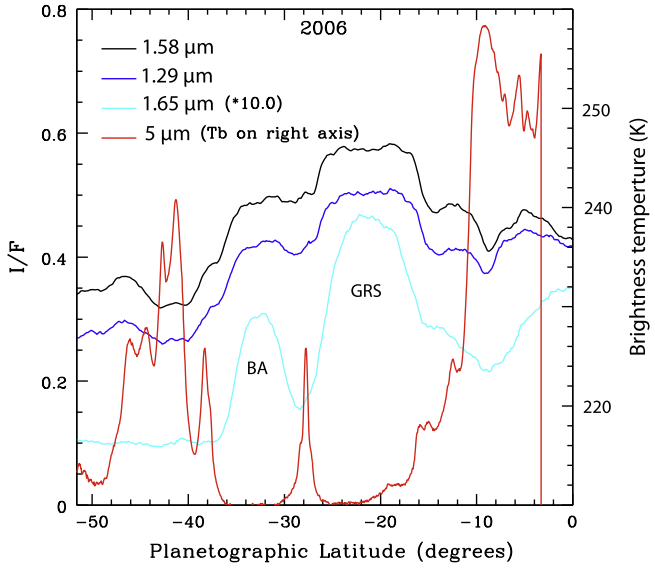

Fig. 14. Latitude scans through the 2006 images at the location of the dashed line in Fig. 12c. The scans at 1.28, 1.58, and 1.65 μm are in units of I/F (left axis; i.e., before conversion to I_0/F with Eq. (1)); the units at 5 μm are in brightness temperature (right axis). We note that the flux density observed in the GRS and Oval BA is about 2% of the peak value observed in the northern hot spot. Since the thermal emission is on the 'Wien slope' of the blackbody (Planck) curve, this flux density translates into a brightness temperature of 200–210 K, and hence the background level when expressed in brightness temperature is artificially high, and cannot be used to constrain the altitude of the centers of any of the ovals. (The web version of this article contains color.)

Fig. 14 shows north–south scans through the GRS and Oval BA in 2006, at several wavelengths (along the dashed line in Fig. 12c). Fig. 15 shows east–west scans through Ovals 2, A5 and A6 in 2008. The anti-correlation between the near-infrared reflectivities and 5-μm thermal emissions is apparent, in particular for the smaller vortices. The brightness temperature at 5 μm typically varies between 225 and 260 K. The temperature in the hot spot along the northern edge of the 2008 map is 261 K; it is about 225 K just south of the GRS and Oval BA; ∼235 K around Oval 2 in 2008, and up to 250 K around Ovals A5 and A6. Physical temperatures of 225 K up to 260 K are reached at pressure levels ranging from 2.5 bar up to slightly over 4 bar (i.e., in the water–ice cloud).

Our 5-μm brightness temperatures are in general consistent with observations from the infrared spectrometers on Voyager-1 (IRIS), the Infrared Space Observatory (ISO/SWS) and from Galileo (NIMS) (Roos-Serote et al., 1999). Although our data are integrated over a bandpass of 0.24 μm, and hence are insensitive to individual water absorption lines, our spatial resolution is over an order of magnitude better than that in the Voyager and ISO data, and a factor of a few higher than in the Galileo NIMS images (assuming 2 pixels per resolution element, the NIMS resolution varied from 600 to 1800 km; Roos-Serote et al., 1998). Roos-Serote et al. (1999) present model fits to the Voyager IRIS spectra, based upon a thermal profile and gas abundances (in the deep atmosphere) as measured by the Galileo Probe. In their model, the ammonia profile follows the saturated vapor curve at higher altitudes, and they adopted a 1% relative humidity for water. Roos-Serote et al. (1999) obtained best fits to their data by adopting two cloud layers: an optically thick layer at 7 bar, and one with a variable opacity at 1.55 bar. These fits match both their measured absolute flux level and spectral shape. The spectral shape constrains their data most. Although our data do not have any spectral resolution, the spatial resolution is very high, so that our 5-μm bright regions may not be contaminated much by cloudy areas, in contrast to the earlier observations. Our data can be modeled well with the Roos-Serote et al. (1999) models containing a partially transparent cloud at 4 bar, or by a model that is cloud-free down to ∼5–7 bar, with an opaque cloud at these deeper levels. Hence, vortices must extend vertically over a large range of altitudes, from 4–7 bar up to the tropopause and perhaps into the lower stratosphere.

5. Discussion

In this paper we focus on ovals in the southern hemisphere at latitudes between ∼20°S and ∼60°S, within about ±45° in longitude from the GRS. In Sections 3 and 4 we showed that vortices are distinct entities both in reflected sunlight and in images of

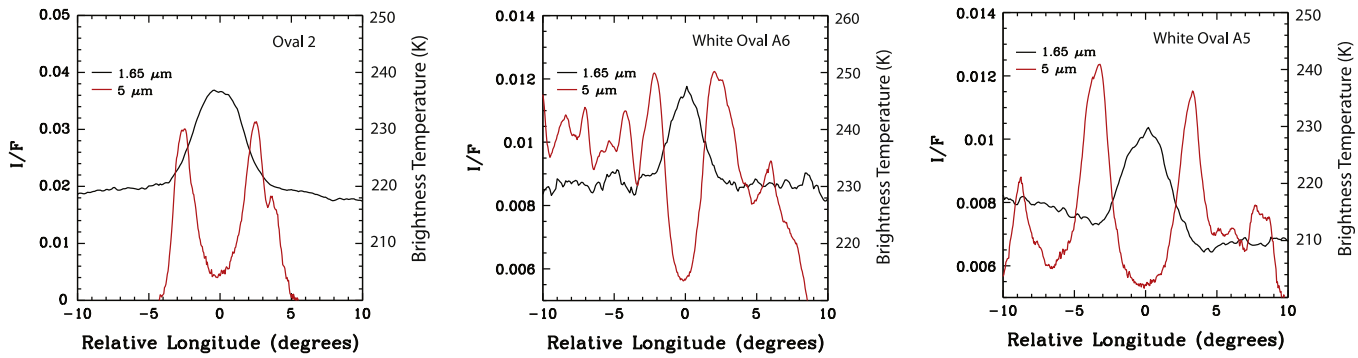

Fig. 15. Longitude scans through Ovals 2, A5 and A6 in 2008, at 1.65 μm and 5 μm (I/F units as in Fig. 14). These two scans show a perfect anti-correlation, as discussed in the text and shown in Fig. 16a. (The web version of this article contains color.)

Jupiter's thermal 5-μm emission. We show that all ovals with diameters <5000–6000 km are surrounded by annular rings that are bright at 5 μm and dark/blue in the visible (Fig. 13). As the brightness temperatures in these rings range from 225 to 250 K, the data indicate cloud-free regions down to at least 4, if not 5–7 bar, i.e., to within the water–ice cloud, while the center of the vortices rise up to well above the tropopause. Below (Section 5.1) we suggest that these 5-μm rings form part of the secondary circulation in a vortex. Although there is 5-μm emission around the largest vortices, Oval BA and the GRS, the morphology of these emissions is distinctly different from that of the smaller ovals, and we argue below that the 5-μm emission near Oval BA and the GRS are not part of their secondary circulations.

The radii of the largest of the 5-μm annuli, ~2500–3000 km, are of order 1–2 times the Rossby deformation radius, L_R, which is ~2300 km at ~23°S and varies with latitude θ as $1/|\sin\theta|$ if the thermal structure is constant (Shetty et al., 2007). The radii of the smaller 5-μm rings at $\gtrsim 50°$S are also $\lesssim 1$–$2L_R$, as well as the radius of the distinctly red annulus of Oval BA ($\sim 1.5L_R$), and the inner core of the GRS, often characterized by an anomalous coloring with respect to the rest of the GRS. In the following subsection we tie these radii to a model of the vertical (secondary) circulation in a vortex. We then use the resulting model to derive the radial mixing time in a vortex to get a handle on the mechanism that produces the red color in Oval BA's annulus. Section 5.2 summarizes our findings on Oval BA. Since the GRS is very different, and we do provide additional observational evidence for this, Section 5.3 provides a short discussion of the GRS.

5.1. General vortex structure and dynamics

Based upon Voyager IRIS observations, Conrath et al. (1981) show that the temperature at the top of the three large white ovals (i.e., those that later merged to become Oval BA) and the GRS (100–400 mbar) is slightly (~1–6 K) lower than the ambient value at the same pressure level (similar results have later been obtained from mid-IR ground-based data; e.g., Cheng et al., 2008; Fletcher et al., 2010). They explain this via adiabatic cooling of parcels of air that rise upwards, driven by an energy source such as latent heat release of condensation. It is not explained, however, why the cores of these clouds do not warm up due to this heat release, as we see on Earth (Kuo, 1965). In the following we agree with the overall picture that rising motions in a subadiabatic atmosphere cool; however, we think that the reason air is rising is baroclinic forcing, as explained below.

All jovian anticyclones in which the velocities have been measured (GRS, Oval BA and its predecessors) have Rossby numbers less than unity:

$$\mathscr{R}_0 = \frac{U}{f_c L} < 1,$$

with U the primary, azimuthal velocity of the oval, f_c the Coriolis parameter, and L the oval's mean radius, defined as the radius of the potential vorticity anomaly. Hence, these ovals must be in geostrophic balance. The smaller vortices are most likely in geostrophic balance as well, with equivalently small Rossby numbers. The mean radius for these ovals is that of the 5-μm bright rings. Although L is often smaller for these high latitude ovals, f_c is larger since these ovals are at higher latitudes. For example, the radius L for Oval A5 is similar to that of Oval BA, and L for Oval A6 is ~1.5 times smaller. However, at these latitudes, f_c is larger by about 20%, so the product $f_c L$ is not very different for Oval BA than for Ovals A5 and A6. While we do not know U, it is hard to imagine that U would be much larger for the small ovals than the larger ones, and thus $\mathscr{R}_0$ must be small for all ovals. This means that all anticyclones have anomalously high pressures in their centers to balance, in the horizontal directions, the Coriolis force (see sketch in Fig. 16a and b). Geostrophic balance also implies that at the top of the vortex, where by definition the horizontal velocity goes to zero, the pressure is equal to the ambient value. Since the temperature at the top of the vortices is lower than the ambient temperature at the same pressure level, the density in the vortex must be higher than in the ambient atmosphere. In the vertical direction, this anomalously high density at the top of the vortex balances the anomalously high pressure at the vortex center (Fig. 16) through hydrostatic equilibrium. As radiation from the surroundings (ultimately from the Sun) tends to warm up the cool parcel at the top of the vortex to the temperature of the ambient gas, its density will be decreased. This imbalance results in gas being pushed (baroclinically) upward to the top of the anticyclone by the high pressure in the vortex center. A parcel cools as it rises adiabatically regardless of whether the surrounding atmosphere is subadiabatic or superadiabatic. If the environment is subadiabatic, the rising parcel will be cooler than the ambient gas when it arrives at the higher elevation. If the ambient atmosphere is superadiabatic (unstable to convection) it will be warmer. If the parcel arriving at the top of an anticyclone were warmer than the ambient gas at that elevation, equilibrium would not be restored. Hence the data show that the atmosphere is subadiabatic.

Clouds can form when the partial pressure of the gas from which they are created exceeds its critical value for a phase transi-

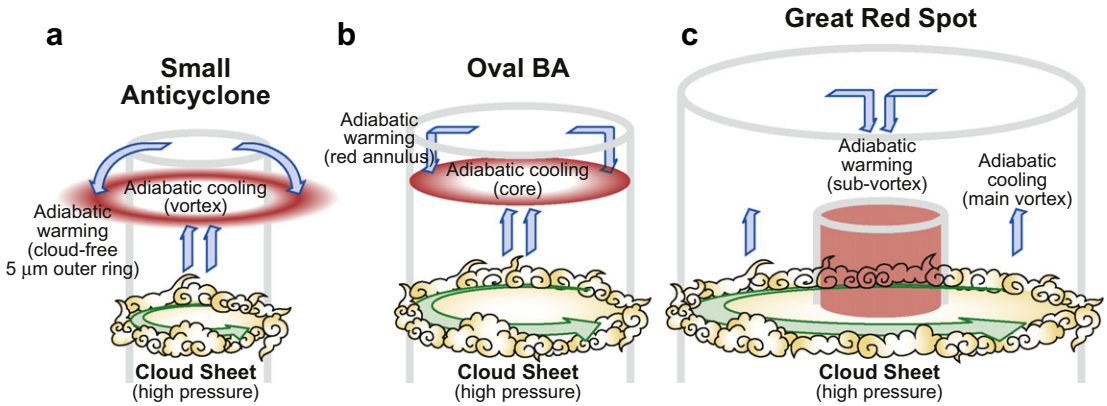

Fig. 16. Sketch of the circulation in three vortices: (a) a small oval (radius of the 5-μm rings <3000 km, and the radius of the clouds that make the oval visible in HST data is roughly half this number); (b) Oval BA, where the clouds extend well beyond the potential vorticity boundary, i.e., the radius of the clouds is >3000 km; (c) the Great Red Spot. Primary circulations are counterclockwise along isobaric contours in a horizontal plane; they are measured in the cloud sheet, as indicated. At present, wind velocity fields can only be measured in the larger anticyclones (BA, GRS). The secondary circulation is primarily in the vertical direction, as indicated by the arrows. The pressure at the center of the vortex (near 2 bar; Section 5.1) is anomalously high, as indicated. (The web version of this article contains color.)

tion to a liquid or a solid. As the critical pressure for melting and sublimation decreases exponentially with decreasing temperature, clouds often form in rising parcels (in the troposphere) and are destroyed in subsiding air, regardless of the lapse rate of the ambient atmosphere. The presence of clouds in vortices thus suggests rising gas, while the most accepted explanation of the anomalously bright 5-μm regions on Jupiter is that they represent cloudless regions where deeper warmer layers in the atmosphere are probed. Thus the bright 5-μm annular rings around the small vortices are likely regions of subsidence.

If vortices are in equilibrium, as their longevity suggests, then what goes up must also come down, i.e., each anticyclone must have sinking parcels as part of its secondary circulation to balance the rising parcels in its core. It is our conjecture that the gas that is rising upward in the vortex must fall back down, and that the 5-μm bright annular rings in our observations (Figs. 12 and 13) are the locations where this gas falls back down. These locations, or equivalently, the radii of the 5-μm bright annuli, depend on the radial velocity of the gas: Once the gas arrives at the upper boundary of the vortex it must radially spread outward (diverge). Unfortunately, the radial velocity within an oval has never been measured directly.

However, we can estimate the velocity by starting with the analysis that was used by Conrath et al. (1981) to obtain their estimate. In Conrath et al.'s work, the observed cool temperature anomaly, ΔT, at the top of the oval is the temperature difference between the fluid in the oval and that of the ambient gas at the same elevation. ΔT is related to the static stability ($dT/dz - dT/dz|_s$) by:

$$-\frac{\Delta T}{\tau_r} = w\left(\frac{dT}{dz} - \left.\frac{dT}{dz}\right|_s\right), \tag{4}$$

where the vertical temperature gradient of an adiabatic (isentropic) atmosphere is:

$$\left.\frac{dT}{dz}\right|_s = -\frac{g}{c_P} = -\frac{R}{c_P}\frac{T}{H},$$

with R the gas constant, H the pressure scale height, τ_r the radiative cooling/warming time, g the jovian gravity, c_P the heat capacity at constant pressure, and w the vertical velocity. When Eq. (4) is multiplied by the density ρ, the vertical half-thickness of the Oval D, and c_P, Eq. (4) becomes the heat flux equation (used, for example, in stellar convection) because $-\rho c_P D(\Delta T)/\tau_r$ is the heat flux into the oval from radiation at the top of the oval.

Although we agree with Eq. (4), we disagree with the value that Conrath et al. used for dT/dz. Conrath et al. set dT/dz equal to the value of the vertical temperature gradient of the mean atmosphere *outside* the oval, $dT/dz|_{outside}$. However, the heat transport described by Eq. (4) is *inside*, and therefore dT/dz should be set equal to $dT/dz|_{inside}$. A non-zero secondary circulation mixes heat within the oval and makes $dT/dz\,|_{outside} \neq dT/dz|_{inside}$, and we show below that if we self-consistently find w and $dT/dz|_{inside}$, then w is much larger than the estimate of Conrath et al.

We can solve for the two unknowns, w and ($dT/dz|_{inside} - dT/dz|_s$), by using a second equation along with Eq. (4). For this we use an energy equation. Note that the density anomaly with respect to the ambient fluid at the top of the oval is $(\Delta\rho) = -\rho(\Delta T)/T$, due to the ideal gas equation and the fact that at the top of the oval, the pressure anomaly (ΔP) is zero. (*n.b.*, at all elevations, the pressure anomaly in the oval is balanced by the Coriolis force at that particular elevation; by definition the top of the oval is where the oval's azimuthal velocity is zero, which makes the Coriolis force and also the pressure anomaly zero at that elevation.) In the top half of the oval and along its central axis, the secondary circulation (i.e., w) lifts low-entropy, cool, dense material from the center of the oval upward to the top to replace the dense material at the top of the oval that is "lost" by the radiative warming of the ΔT anomaly at the top of the oval. For the vertical velocity to lift a mass $(DL^2)(\Delta\rho)$ upward a distance D in a time τ_r requires an energy input rate of:

$$\dot{E} = (DL^2)(\Delta\rho)\left(\frac{g_e D}{\tau_r}\right) = -(DL^2)\left(\frac{\rho\Delta T}{T}\right)\left(\frac{g_e D}{\tau_r}\right), \tag{5}$$

where L is the mean radius where the flow subsides rather than rises (e.g., mean radius of the 5-μm rings around the smaller vortices), (DL^2) is the volume of the upper part of the oval, and g_e is the effective gravity of the stratified fluid inside the oval (Pedlosky, 1987)

$$g_e \equiv \frac{gH}{T}\left(\left.\frac{dT}{dz}\right|_{inside} - \left.\frac{dT}{dz}\right|_s\right). \tag{6}$$

The energy required to lift the heavy fluid is supplied by the high pressure anomaly (ΔP) at the center of the oval. If there were no radiative cooling/warming and no secondary circulation, then the oval would be in equilibrium: the horizontal gradient of the pressure anomaly would quasigeostrophically balance the Coriolis (and small centrifugal) force and the vertical gradient of the pressure anomaly (ΔP) located at the vortex center would be in hydrostatic equilibrium with the density anomaly $\Delta\rho$, such that

$$(\Delta P) = Dg(\Delta\rho). \tag{7}$$

Due to the radiative warming of the density anomaly at the top of the oval, $(\Delta\rho)$ is slightly smaller than its equilibrium value, or equivalently, the pressure anomaly (ΔP) at the center of the oval is slightly larger than its equilibrium value by an amount δP. It is this pressure δP that drives the secondary flow and supplies the required $\dot{E}$. The force due to this pressure is $L^2(\delta P)$, and the rate at which work is done by this force is $wL^2(\delta P)$. Equating this rate of work with the required $\dot{E}$ from Eqs. (5) and (6) gives

$$w(\delta P) = -D^2 H\frac{(\Delta T)\rho g}{T^2\tau_r}\left(\left.\frac{dT}{dz}\right|_{inside} - \left.\frac{dT}{dz}\right|_s\right). \tag{8}$$

Finally, we note that the radial gradient of (δP) or $(\delta P)/L$ is balanced by the radial component of the inertial term in Euler's equation $\rho(\mathbf{V}\cdot\nabla)\mathbf{V}$, where $\mathbf{V}$ is the velocity of the secondary circulation. The radial component of that term is approximately $\rho v^2/L$, where v is the radial component of $\mathbf{V}$. Therefore,

$$(\delta P) = \rho v^2. \tag{9}$$

Note that because the flow is nearly divergence-free, $v \simeq wL/D$. Multiplying Eq. (8) by w/ρ and using Eqs. (4) and (9), we obtain:

$$v = \sqrt{\left(\left|\frac{\Delta T}{T}\right|\frac{L}{\tau_r}\right)}(gH)^{1/4} \simeq 1\ \mathrm{m/s}, \tag{10}$$

where we used the values of $g = 25\ \mathrm{m\ s^{-2}}$, $H = 20$ km, $\tau_r = 10^8$ s, $L = 3000$ km, and $(|\Delta T|)/T = 0.04$. Note that the mixing time within the oval is defined to be $\tau_{mix} \equiv 4D/w = 4L/v$, and Eq. (10) shows that it is of order several months.

We can determine the vertical aspect ratio D/L of the potential vorticity anomaly of Oval BA (which is not necessarily the same aspect ratio of the cloud associated with the anomaly) from the thermal wind equation, which states that

$$\frac{\Delta T}{T} = \frac{f_c U L}{gD}. \tag{11}$$

Thus, the aspect ratio is $[T/(\Delta T)](f_c U/g)$.[2] Using $(\Delta T)/T = 0.04$, $U = 100\ \mathrm{m\ s^{-1}}$, $f_c = 1.92\times10^{-4}\ \mathrm{s^{-1}}$, we obtain $D/L = 0.02$ and

[2] The Boussinesq equivalent of this expression of the vertical aspect ratio has recently been verified in laboratory experiments of long-lived pancake vortices in rotating, stratified flows (Aubert, 2010).

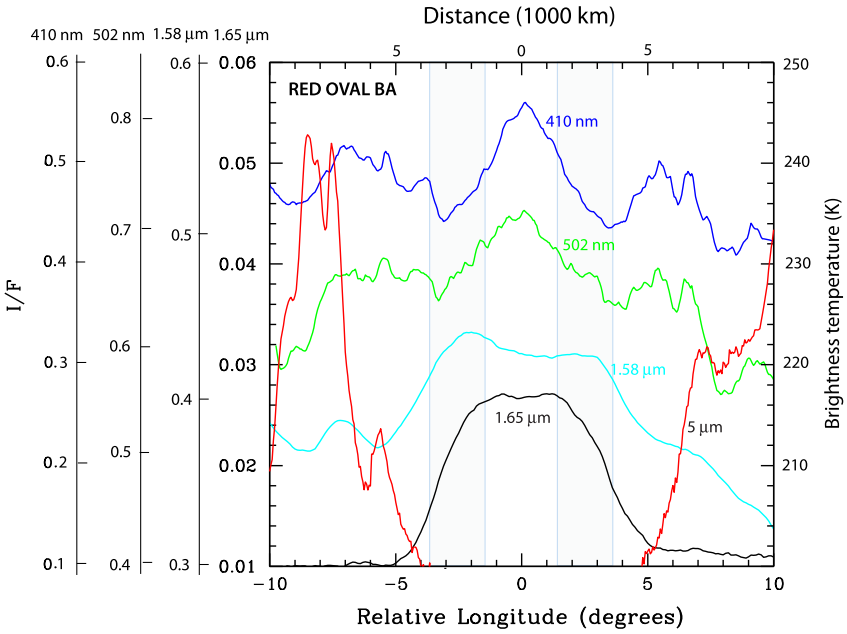

Fig. 17. East–west scans through the Red Oval BA in May 2008. Scans are taken through HST images at 410 and 502 nm, and through Keck AO images at 1.58, 1.65 and 5 μm. The left axis shows the I/F for all images (as indicated); the right axis shows the brightness temperature for the 5-μm map. The light grey regions show the approximate position and extent of the red annulus. The outer boundary of the annulus coincides with the peak velocity in the horizontal wind (Fig. 6b; Asay-Davis et al., 2009). Note that the location of the red annulus relative to the 1.65 μm reflectivity is similar to the location of the 5-μm rings in Fig. 15, as expected if these features are caused by the subsiding (return) flow of the secondary circulation. In contrast, the 5-μm emission in this figure is well outside the 1.65 μm reflectivity of Oval BA, suggesting that these emissions do not form part of the secondary circulation.

D = 60 km. If the vortex top is near 150 mbar (Section 4), then the midplane of the vortex (where the horizontal temperature gradient $\Delta T = 0$) is near 2 bar. To first approximation, the thermal wind equation thus suggests that the dynamical midplane of Oval BA is close to or somewhat deeper than the clouds tracked in visible imaging.

In jovian vortices there are two horizontal length scales that dominate most of the fluid dynamics. One is the characteristic radius of the vortex, and the other is the Rossby deformation radius, L_R, which is the characteristic length scale over which the effects of the Coriolis force are balanced by the buoyancy forces in a geostrophic flow (cf. Pedlosky, 1987). For example, upwelling gas that is thrown radially outward at the top of a vortex with the velocity of an internal gravity (or Poincare) wave will stop moving outward when it reaches an annulus of radius L_R (Gill, 1982). Some jovian vortices are bigger, and others are smaller than L_R. The maximum north–south extent of a jovian anticyclone depends on the latitudinal width of the belt or zone in which it is embedded: an anticyclone can only extend a finite distance into the neighboring cyclonic belts. Most jovian anticyclones, though, are smaller than this maximum size.

Our observations of the small ovals at latitudes between 20°S and ~60°S suggest that the radius of the secondary circulation in those vortices coincides with the radius of the vortex, as indicated by their 5-μm bright annuli, which are indicative of the subsiding part of the circulation. Our observations show that this radius is never larger than $\sim 2L_R$. Vortices which are *much larger* than $\sim 2L_R$, such as the GRS and Oval BA, do not show 5-μm bright annuli around their periphery.[3] The radius of the secondary circulation in these vortices must be *inside* the vortex. Because the visibly red ring in Oval BA is inside the oval with a radius similar to that of the 5-μm bright rings around Ovals 2, A5 and A6, it is plausible that this red annulus is coincident with the subsiding part of the secondary circulation (Fig. 16b). We hypothesize that the radius of the annular feature in the clouds of a jovian anticyclone is the smaller of (1) ~2× the deformation radius or (2) the outer radius of the vortex.

5.2. Red annulus in oval BA

To further investigate Oval BA, Fig. 17 shows east–west scans through this oval as observed in 2008. Scans are shown through HST images at 410 and 502 nm, and through Keck AO images at 1.58, 1.65 and 5 μm. The light grey areas correspond approximately to the position and extent of the red annulus; the outer boundary coincides with the peak velocity in the horizonal wind field. The reflectivity in the HST data is much lower in the ring than at the center of the oval, while the reverse is true in the infrared at 1.58 μm. The methane band image at 1.65 μm shows the vortex to be confined to just the inner region. In contrast to the smaller ovals (e.g., Fig. 15), Oval BA's 5-μm brightness is located at a much larger distance from the edge of the methane band feature, and hence the secondary circulation must be different in Oval BA. As discussed above, we suggest that the descending part of the secondary circulation is within Oval BA, at the location of the red annulus, which is at approximately the same distance from the oval's center as the 5-μm bright rings around Ovals 2, A5 and A6. Support for this hypothesis is given by Cheng et al.'s (2008) temperature maps as derived from mid-IR data: as shown in their Fig. 3, the core of Oval BA is the coldest area between 200 and 400 mbar, and is surrounded by a slightly ($\gtrsim$ 1 K) warmer collar. This higher temperature in the collar might be consistent with adiabatic heating due to subsiding motions in the secondary circulation, as proposed in this paper. (Note that we do not refer here to the much warmer cyclonic area just south – and outside – of Oval BA.)

To further explore the cause of Oval BA's red color, we need to consider the various timescales that govern both the dynamics and

[3] Our observations show 5-μm bright regions that are far outside Oval BA and GRS. These regions have small arc lengths compared to the circumferences of these vortices and they do not form complete annuli. While the 5-μm bright arcs are indicative of descending motion, we think that their locations are not related to the secondary circulations of anticyclones, but rather to the complex interaction between the ambient zonal flows and the vortices.

coloration of Oval BA. The longest relevant timescale is the radiative relaxation time, which is about 4–5 years in the upper troposphere (~0.1–1 bar; Conrath et al., 1990). We have just shown that the timescale for the secondary circulation, the mixing time, is on the order of several months. This is much faster than previous estimates for the mixing time, but much longer than the turnaround time of the vortex, which is about two days as determined from the velocity fields in Asay-Davis et al. (2009).

If the coloration is due to particulates being dredged up directly from deeper layers, the center of the oval should be colored red before the rest of the oval. In fact, as mixing happens on a timescale of months, the oval should now, more than 4 years after its color change, be red throughout. Instead, the red color is concentrated in an annulus and did not appear to have started at the center, nor did the color get mixed throughout the vortex despite the short mixing time.

García-Melendo et al. (2009) compare Oval BA's morphology and color to a map of its potential vorticity (PV), calculated via numerical simulations using the General Circulation Model EPIC (Dowling et al., 1998). They suggest the red annulus coincides with a local minimum in PV, and that steep gradients in PV prevent lateral mixing of the red particulates. Hence, they argue that if the particulates are confined to the low-PV annulus, they would most likely stay there. However, their simulations show that the PV anomaly of the annulus is a short-lived transient, and our measurements of the velocities in Oval BA show that the azimuthal velocity is nearly a linear function of radius without sharp PV gradients (Asay-Davis et al., 2009). Hence we think that this confinement mechanism is not the reason the red color remains confined to an annulus; in addition, it does not explain where the red color comes from.

We therefore conclude that the red color must be produced locally, most likely caused by the adiabatic heating in the subsiding part of the secondary circulation. West et al.'s (1986) two leading models for any red color in Jupiter's atmosphere are (i) "hiding" and "exposing" red chromophores, and (ii) photochemical production of red chromophores. Both of these mechanisms are temperature-sensitive. Timescales relevant to the coloration of the oval by either one of them must be compared to the radial advection timescale – the time needed for the secondary circulation to drive material from the core of the vortex to its edge. Based on its mean radius of ~3000 km and the secondary circulation velocity of 1 m s^{-1}, the radial advection timescale is about one month. For sublimation of ice mantles to reveal red chromophores in Oval BA, the sublimation timescale must be shorter than the radial advection timescale. Sub-micron particles in Jupiter's ammonia cloud have condensation/sublimation times on the order of seconds (Carlson et al., 1988), effectively instantaneous compared with the radial advection timescale. Timescales for photochemical production of red chromophores are unknown. However, once produced, it is unlikely these chromophores will be destroyed, unless they reach much higher temperatures and pressures while mixed throughout the vortex.[4] In a closed system, with a mixing time of about 4–5 months, one might argue that if the red color is the result of an enhanced production rate of red chromophores, the oval should now, more than 4 years later, be red throughout. Hence, if the system can be considered closed, i.e., if the external mixing is slow compared to the advection time, one might argue that the longevity of the red annulus is suggestive of being driven by West et al.'s hiding/exposing mechanism.

[4] Chromophores evaporate at temperatures that exceed their sublimation/condensation temperature. However, as we do not know their composition, their vapor pressure curves are unknown, and hence we do not know to which depths chromophores can exist.

5.3. The Great Red Spot

The morphology (in shape and color) of the GRS and its wind velocity field are very different from any of the other vortices. The radius of the dark-red core of the GRS is similar to that of the 5-μm bright rings around several vortices and to the Rossby deformation radius. As shown in several papers, each based on different datasets, there is essentially no wind, possibly even a small counter-rotation, across the dark core of the GRS (e.g., Mitchell et al., 1981; Choi et al., 2007; Asay-Davis et al., 2009); the absence of wind is also referred to as the GRS being "hollow" (Shetty et al., 2007; Shetty and Marcus, 2010). Fletcher et al. (2010) published a detailed paper on the thermal structure and composition of the GRS as derived from mid-IR observations. Consistent with Voyager observations (Conrath et al., 1981), the vortex is cold in the upper troposphere (~100–500 mbar). Fletcher et al. (2010) show that the dark-red core is warmer (by 1–1.5 K in the east–west direction) than the rest of the GRS. The authors further compare maps of para-H_2 with the equilibrium para-H_2 fractions one would expect based upon the temperature profile the authors had extracted from their data. A minimum in the para-H_2 fraction, which translates into a maximum in the disequilibrium (i.e., sub-equilibrium) values, is present over the GRS, in agreement with previous Voyager/IRIS measurements (Sada et al., 1996; Simon-Miller et al., 2002). However, sub-equilibrium is confined to the area around the dark-red core (but inside the location of the peak values in the local wind velocity field), while para-H_2 inside the core seems the be more or less in equilibrium. Sub-equilibrium conditions are brought about if gas is rising upwards, while super-equilibrium indicates strong subsidence – i.e. the motions of the gas must be faster than the equilibration time to be in disequilibrium.

Based upon Fletcher et al.'s mid-IR measurements we suggest a secondary circulation scheme for the GRS that is very different from that of the other vortices, but has the horizontal length scale, $\sim L_R$, in common. This circulation is sketched in Fig. 16c: gas is rising in an annulus surrounding the dark-red core of the GRS, and descending (at least in part) over the dark-red core, where adiabatic compression heats the gas. The dark-red color and the subsiding motions here can be compared directly to the processes that colored the annulus in Oval BA red. Although it is possible that part of the rising air in the secondary circulation descends at larger, rather than smaller, radii from the center, our observations do not show clear evidence of this. However, from Fletcher et al.'s (2010) work it is clear that the overall dynamics in and near the GRS is very complex. The secondary circulation described here is clearly part of a much larger and more complex dynamical system.

6. Conclusions

In order to get a better understanding of the mechanism that results in Oval BA's red annulus, we observed differently sized anticyclones in Jupiter's atmosphere. With these data we were able to constrain, observationally, the vertical structure of and secondary circulation in vortices. A comparison of this variety of vortices leads us to conclude that the red color in Oval BA's red annulus is best explained via the oval's secondary circulation pattern, with gases rising along the center of the vortex and descending at the location of the red annulus. We developed a theory for the secondary circulation, which provides us with an estimate for the radial mixing time in the oval. As this timescale is of order several months, and the red annulus has been stable for over 4 years, we suggest that the red color of Oval BA's annulus must be produced locally, most likely triggered by adiabatic heating in the subsiding part of the secondary circulation. Of the two mechanisms that would produce a red color in an environment with a higher-than-normal temperature, we favor West et al.'s (1986) model of

"hiding" and "exposing" chromophores via condensation and sublimation of NH_3–ice, although an increase in the photochemical production rate of red chromophores cannot be excluded if the external mixing time is fast, i.e., similar to the mixing time.

In the following we provide a summary of the (i) observational and (ii) theoretical aspect of the research that culminated in the above conclusion.

(i) We presented observations of Jupiter taken in reflected sunlight with the Keck AO system at 1.1–1.8 μm and with HST at 250–890 nm. These datasets were complemented with Keck AO observations at 5 μm, sensitive to Jupiter's thermal emission from its deep atmosphere. While the images in reflected sunlight provide information on the clouds/hazes in the troposphere–stratosphere, the thermal emission maps were used to extract information on Jupiter's deep atmosphere. We used these complementary datasets to derive, observationally, the vertical structure and secondary circulation patterns of various sized vortices, such as the GRS, Oval BA, the smaller Ovals 2, A5 and A6, and the tiny ovals between 45°S and 60°S. The vertical structure of the five largest vortices (GRS, BA, Ovals 2, A5, A6) can be modeled by three haze layers above the NH_3–ice cloud (at 700–750 mbar): a layer in the lower stratosphere–tropopause at 2–200 mbar, an upper tropospheric layer at 200–650 mbar and a third (denser) layer just above the ammonia-ice cloud at 650–700 mbar. The high reflectivities of the GRS, Oval BA and Oval 2 at 892 nm and 1.65 μm can only be explained by a relatively high particle density in the top two layers. The particle densities in the two white Ovals, A5 and A6, are smaller by a factor of ~5–8. Numerous tiny ovals exist between 45°S and 60°S; at 5 μm, rings with diameters $\lesssim$1000 km can be discerned around their visible counterparts in HST data. The Ovals 2, A5 and A6 are also surrounded by bright (225–250 K) rings at 5 μm, indicative of annuli around the periphery of the ovals (the periphery of the clouds that make the ovals visible) that are cloud-free down to at least ~4 bar, and perhaps to 5–7 bar. We therefore suggest the anticyclones to extend vertically from (at least) the water cloud (~5 bar) up to the tropopause (~100–200 mbar), and in some cases into the stratosphere. The 5-μm bright rings coincide with the dark/blue rings that surround the ovals at visible wavelengths. Although high brightness temperatures are seen at some places around Oval BA and the GRS, there are no complete rings around their periphery as around smaller vortices, and hence the 5-μm emissions outside Oval BA and the GRS are not part of the secondary circulations within the vortices.

(ii) We re-evaluated the secondary circulation model developed by Conrath et al. (1981), and propose instead that air is (baroclinically) rising along the center of all (except the GRS) vortices in a subadiabatic atmosphere, and descending at a distance not much exceeding ($\lesssim 2\times$) the local Rossby deformation radius. Using the 5-μm bright rings around the largest of the small ovals, Ovals 2, A5 and A6, we constrain this maximum radius of the secondary circulation observationally to $\lesssim$3000 km, which is always less then $\sim 2L_R$. For the larger ovals, the return flow must be inside the oval, i.e., inside the clouds that make the oval visible. We suggest that the return flow in Oval BA is at the location of this oval's red annulus, which is located at the maximum observed distance of return flows around smaller vortices.

We further show that the radial mixing time in a vortex is of order several months, rather than several years to a decade as proposed by Conrath et al. (1981). This difference is caused by different values used for the vertical temperature gradient: the latter authors used the temperature gradient of the mean atmosphere outside the oval, while we use that inside the oval, as appropriate for calculations inside the oval. With a mixing time this fast, Oval BA should be colored red throughout by now, more than 4 years after its color change, unless the red color of Oval BA's annulus is produced locally. One likely production scenario is sublimation of NH_3–ice as the temperature within the annulus is raised through adiabatic compression. Sublimation of the ice exposes the condensation nuclei, i.e., the red chromophores (West et al., 1986). Radial migration and/or uplift will carry the chromophores into colder areas, and subsequent condensation of NH_3 onto these condensation nuclei will hide them from view. Another plausible mechanism is enhanced production of red chromophores, as the chemical pathways leading to these chromophores are a steep function of temperature. If we are dealing with a closed system, or a system where the external mixing rate is slow compared to the mixing time of 4–5 months, one would expect the oval to be colored red throughout in less than 4 years unless the red chromophores are destroyed on a timescale short compared to the mixing time (which we argue is unlikely), or if they are covered by ice as in the hiding/exposing mechanism above.

Despite the fact that we provide the reader with a consistent theory of the vertical structure and secondary circulation in vortices, we encourage observers, experimenters, and theorists to test our (dynamical) model via more observations, laboratory experiments, and numerical simulations. In particular, although we think that the red color in Oval BA is best explained through a combination of the secondary circulation dynamics with the hiding/exposing and/or photochemical models, we still do not know how to explain red colors on Jupiter in a general way. For this we need to understand what the chromophores are (composition), where they come from in the first place (what are their precursors, if produced via photochemistry and subsequent chemical pathways), and where they go, i.e., what their life cycle is.

As the secondary circulation must have existed in White Oval BA, as well as in the white ovals before they merged, one may ask the question why it took 5–6 years before the Oval turned red. It is possible, as argued by Marcus (2004), that the merging of the white ovals prevented large-scale mixing of heat across the 33°S latitude band, i.e., that this latitude became a barrier to the meridional transport of heat. The net result of such a barrier is that over a thermal timescale Jupiter's atmosphere would heat up by several degrees at latitudes north (equatorward) of ~33°S. Such a global increase in temperature might have "exposed" chromophores which used to be covered by NH_3 ice.

Acknowledgments

We thank K. Baines for providing the Cassini VIMS spectrum to check our photometric calibration, and two anonymous referees, as well as editor A. Ingersoll, to help improve the paper. In addition, we did benefit from Email exchanges with J. Moses, R. West and D. Strobel. The near-infrared data were obtained with the W.M. Keck Observatory, which is operated by the California Institute of Technology, the University of California, and the National Aeronautics and Space Administration. The Observatory was made possible by the generous financial support of the W.M. Keck Foundation. The visible wavelength data were obtained with the NASA/ESA Hubble Space Telescope. These observations are associated with HST Programs GO/DD 10782 and GO 11102, with support provided by NASA through a grant from the Space Telescope Science Institute, which is operated by the Association of Universities for Research in Astronomy, Inc., under NASA Contract NAS 5-26555. This work was further supported in part by the National Science Foundation Science and Technology Center for Adaptive Optics,

managed by the University of California at Santa Cruz under cooperative agreement AST 98-76783, as well as the NSF TerraGrid Center. Support was further provided by the Berkeley–France Fund, NSF award AST-0808200, and NASA Award #NNX10AB93G to the University of California, Berkeley. We benefitted greatly from the use of JPL's Horizons system and SETI's Planetary Rings Node. The authors extend special thanks to those of Hawaiian ancestry on whose sacred mountain we are privileged to be guests. Without their generous hospitality, none of the observations presented would have been possible.

References

Ádámkovics, M., de Pater, I., Hartung, M., Eisenhauer, F., Genzel, R., Griffith, C.A., 2006. Titan's bright spots: Multiband spectroscopic measurement of surface diversity and hazes. J. Geophys. Res. 111, EO7S06.

Ádámkovics, M., Wong, M.H., Laver, C., de Pater, I., 2007. Detection of widespread morning drizzle on Titan. Science 318, 962–965.

Asay-Davis, X.S., Marcus, P.S., Wong, M.H., de Pater, I., 2009. Jupiter's evolving Great Red Spot: Velocity measurements with the advection corrected correlation image velocimetry automated cloud tracking method. Icarus 203, 164–188.

Aubert, O., 2010. Form and persistence of a vortex in a rotating and stratified fluid. Master thesis, Fluid Mechanics, Fundamentals and Applications. École Polytechnique, France.

Banfield, D., Gierasch, P.J., Bell, M., Ustinov, E., Ingersoll, A.P., Vasavada, A.R., West, R.A., Belton, M.J.S., 1998. Jupiter's cloud structure from Galileo imaging data. Icarus 135, 230–250.

Borysow, A., 1991. Rotovibrational collision-induced absorption spectra of H_2–H_2 pairs in the fundamental band ($0 \rightarrow 1$) at temperatures from 20 to 300 K. Icarus 92, 273–279.

Borysow, J., Frommhold, L., Birnbaum, G., 1988. Collision-induced rototranslational absorption spectra of H_2–He pairs at temperatures from 40 to 3000 K. Astrophys. J. 326, 509–515.

Bowles, N., Calcutt, S., Irwin, P., Temple, J., 2008. Band parameters for self-broadened ammonia gas in the range 0.74 to 5.24 m to support measurements of the atmosphere of the planet Jupiter. Icarus 196, 612–624.

Carlson, B.E., Rossow, W.B., Orton, G.S., 1988. Cloud microphysics of the giant planets. J. Atmos. Sci. 45, 2066–2081.

Cheng, A.F., and 14 colleagues, 2008. Changing characteristics of Jupiter's Little Red Spot. Astron. J. 135, 2446–2452.

Choi, D., Banfield, D., Gierasch, P., Showman, A., 2007. Velocity and vorticity measurements of Jupiter's Great Red Spot using automated cloud feature tracking. Icarus 188, 35–46.

Colina, L., Bohlin, R.C., Castelli, F., 1996. The 0.12–2.5 micron absolute flux distribution of the Sun for comparison with solar analog stars. Astron. J. 112, 307–315.

Conrath, B.J., Flasar, F.M., Pirraglia, J.A., Gierasch, P.J., Hunt, G.E., 1981. Thermal structure and dynamics of the jovian atmosphere. 2. Visible cloud features. J. Geophys. Res. 86, 8769–8775.

Conrath, B.J., Gierasch, P.J., Leroy, S.S., 1990. Temperature and circulation in the stratosphere of the outer planets. Icarus 83, 255–281.

de Pater, I., Dunn, D., Zahnle, K., Romani, P.N., 2001. Comparison of Galileo Probe data with ground-based radio measurements. Icarus 149, 66–78.

de Pater, I., Marchis, F., Macintosh, B.A., Roe, H.G., Le Mignant, D., Graham, J.R., Davies, A.G., 2004. Keck AO observations of Io in and out of eclipse. Icarus 169, 250–263.

de Pater, I., DeBoer, D.R., Marley, M., Freedman, R., Young, R., 2005. Retrieval of water in Jupiter's deep atmosphere using microwave spectra of its brightness temperature. Icarus 173, 425–438.

de Pater, I., Hammel, H., Fletcher, L., Orton, G., Pérez-Hoyos, S., Wong, M.H., Luzscz-Cook, S., Sánchez-Lavega, A., Boslough, M., 2010. A multi-wavelength study of the 2009 impact on Jupiter: Comparison of high resolution images from Gemini, Keck and HST. Icarus, in press, doi:10.1016/j.icarus.2010.07.010.

Dowling, T.E., Fischer, A.S., Gierasch, P.J., Harrington, J., LeBeau, R.P., Santori, C.M., 1998. The explicit planetary isentropic-coordinate (EPIC) atmospheric model. Icarus 132, 221–238.

Elias, J.H., Frogel, J.A., Matthews, K., Neugebauer, G., 1982. Infrared standard stars. Astron. J. 87, 1029–1034.

Fletcher, L.N.13 colleagues, 2010. Thermal structure and composition of Jupiter's Great Red Spot from high-resolution thermal imaging. Icarus 208, 306–318.

García-Melendo, E., Legarreta, J., Sánchez-Lavega, A., Hueso, R., Pérez-Hoyos, S., González, J., Gómez-Forrellad, J.M., and IOPW Team, 2009. The jovian anticyclone BA: I. Motions and interaction with the GRS from observations and non-linear simulations. Icarus, 203, 486–498.

Gill, A., 1982. Atmosphere-Ocean Dynamics. International Geophysics Series, vol. 30. Academic Press, Orlando, FL.

Go, C., de Pater, I., Wong, M., Lockwood, S., Marcus, P., Asay-Davis, X., Shetty, S., 2006. Evolution of the Oval BA during 2004–2005. Bull. Am. Astron. Soc. 38, 495.

Hammel, H.B., Baines, K.H., Bergstrahl, J.T., 1989. Vertical aerosol structure of Neptune: Constraints from center-to-limb profiles. Icarus 80, 416–438.

Hansen, J.E., Travis, L.D., 1974. Light scattering in planetary atmospheres. Space Sci. Rev. 16, 527–611.

Hueso, R., Legarreta, J., Garcia-Melendo, E., Sanchez-Lavega, A., Perez-Hoyos, S., 2009. The jovian anticyclone BA: II. Circulation and interaction with the zonal jets. Icarus 203, 499–515.

Ingersoll, A.P., 1990. Atmospheres of the giant planets. In: Beatty, J.K., Chaikin, A. (Eds.), The New Solar System, third ed. Sky Publishing Corp., Cambridge, MA, pp. 139–152.

Irwin, P.G.J., Sromovsky, L.A., Strong, E.K., Sihra, K., Teanby, N.A., Bowles, N., Calcutt, S.B., Remedios, J.J., 2006. Improved near-infrared methane band models and k-distribution parameters from 2000 to 9500 cm^{-1} and implications for interpretation of outer planet spectra. Icarus 181, 309–319.

Karkoschka, E., 1994. Spectrophotometry of the jovian planets and Titan at 300 to 1000 nm wavelength: The methane spectrum. Icarus 111, 174–192.

Kuo, H.L., 1965. On the formation and intensification of tropical cyclones through latent heat release by cumulous convection. J. Atmos. Sci. 22, 40–63.

Lii, P.S., Wong, M.H., de Pater, I., 2010. Temporal variation of the tropospheric cloud and haze in the jovian equatorial zone. Icarus 209, 591–601.

Luszcz-Cook, S., de Pater, I., Ádámkovics, M., Hammel, H.B., 2010. Seeing double at Neptune's south pole. Icarus 208, 938–944.

Marcus, P.S., 2004. Prediction of a global climate change on Jupiter. Nature 428, 828–831.

Marcus, P., Asay-Davis, X., Wong, M.H., Go, C., de Pater, I., 2007. Jupiter's new red oval – Its relation to global changes. Bull. Am. Astron. Soc. 39, 408.

Martonchik, J.V., Orton, G.S., Appleby, J., 1984. Optical properties of NH_3 ice from the far infrared to the near ultraviolet. Appl. Opt. 23, 541–547.

Mitchell, J.L., Beebe, R.F., Ingersoll, A.P., Garneau, G.W., 1981. Flow fields within Jupiter's Great Red Spot and White Oval BC. J. Geophys. Res. 86, 8751–8757.

Munoz, O., Moreno, F., Molina, A., Ortiz, J.L., 1999. A comparison of the structure of the aerosol layers in the Great Red Spot of Jupiter and its surroundings before and after the 1993 SEB disturbance. Astron. Astrophys. 344, 355–361.

Pavlovsky, C., Koekemoer, A., Mack, J., 2006. ACS Data Handbook, Version 5.0. Space Telescope Science Institute, Baltimore, MD.

Pedlosky, J., 1987. Geophysical Fluid Dynamics. Springer-Verlag, New York.

Peek, B.M., 1958. The Planet Jupiter. Faber and Faber, London.

Pérez-Hoyos, S., Sánchez-Lavega, A., Hueso, R., García-Melendo, E., Legarreta, J., 2009. The jovian anticyclone BA: III. Aerosol properties and color change. Icarus 203, 516–530.

Persson, S.E., Murphy, D.C., Krzeminski, W., Roth, M., Rieke, M.J., 1998. A new system of faint near-infrared standard stars. Astron. J. 116, 2475–2488.

Rayner, J.T., Cushing, M.C., Vacca, W.D., 2009. The IRTF Spectral Library: Cool stars. Astrophys. J. Suppl. 185, 289–432. <http://irtfweb.ifa.hawaii.edu/~spex/IRTFSpectralLibrary/>.

Rogers, J.H., Mettig, H.-J., 2008. Influence of Jupiter's south equatorial disturbance on jetstream speed. J. Br. Astron. Assoc. 118, 326–334.

Roos-Serote, M., and 12 colleagues, 1998. Analysis of Jupiter north equatorial belt hot spots in the 4–5-μm range from Galileo/near-infrared mapping spectrometer observations: Measurements of cloud opacity, water, and ammonia. J. Geophys. Res. 103, 23023–23042.

Roos-Serote, M., Drossart, P., Encrenaz, Th., Carlson, R.W., Leader, F., 1999. Constraints on the tropospheric cloud structure of Jupiter from spectroscopy in the 5-μm region: A comparison between Voyager/IRIS, Galileo-NIMS, and ISO-SWS spectra. Icarus 137, 315–340.

Sada, P.V., Beebe, R.F., Conrath, B.J., 1996. Comparison of the structure and dynamics of Jupiter's Great Red Spot between the Voyager 1 and 2 encounters. Icarus 119, 311–335.

Sanchez-Lavega, A., Rojas, J.F., Hueso, R., Lecacheux, J., Colas, F., Acarreta, J.R., Miyazaki, I., Parker, D., 1999. Interaction of jovian White Ovals BC and DE in 1998 from Earth-based observations in the visual range. Icarus 142, 116–124.

Sanchez-Lavega, A., and 12 colleagues, 2001. NOTE: The merger of two giant anticyclones in the atmosphere of Jupiter. Icarus 149, 491–495.

Sanchez-Lavega, A., Legarreta, J., Garcia-Melendo, E., Gomez, J.M., Perez-Hoyos, S., Hueso, R., Orton, G.S., and IOPW Team, 2008. Observations and models of the interaction of a large red oval with the Great Red Spot in June–July 2008. Bull. Am. Astron. Soc. 40, 487.

Seiff, A., Kirk, D.B., Knight, T.C.D., Young, R.E., Mihalov, J.D., Young, L.A., Milos, F.S., Schubert, G., Blanchard, R.C., Atkinson, D., 1998. Thermal structure of Jupiter's atmosphere near the edge of a 5-m hot spot in the north equatorial belt. J. Geophys. Res. 103, 22857–22890.

Shetty, S., Marcus, P.S., 2010. Changes in Jupiter's Great Red Spot (1979–2006) and Oval BA (2000–2006). Icarus, in press, doi:10.1016/j.icarus.2010.05.026.

Shetty, S., Asay-Davis, X.S., Marcus, P.S., 2007. On the interaction of Jupiter's Great Red Spot and zonal jet streams. J. Atmos. Sci. 64, 4432–4444. doi:10.1175/2007JAS2097.1.

Simon-Miller, A., Gierasch, P., Beebe, R., Conrath, B., Flasar, F., Achterberg, R., 2002. New observational results concerning Jupiter's Great Red Spot. Icarus 158, 249–266.

Simon-Miller, A.A., Chanover, N.J., Orton, G.S., Sussman, M., Tsavaris, I.G., Karkoschka, E., 2006. Jupiter's white oval turns red. Icarus 185, 558–562.

Spencer, J.R., Carlson, R.W., Becker, R.W., Blue, J.S., 2004. Maps and spectra of Jupiter and the Galilean satellites. In: Bagenal, F., Dowling, T.E., McKinnon, W. (Eds.), Jupiter: Planet, Satellites & Magnetosphere. Cambridge University Press, Cambridge, UK, pp. 700–709.

Terrile, R.J., Capps, R.W., Becklin, E.E., Cruikshank, D.P., 1979. Jupiter's cloud distribution between the Voyager 1 and 2 encounters: Results from 5-micrometer imaging. Science 206, 995–996.

Tody, H., 1993. IRAF in the nineties. In: Hanisch, R.J., Brissenden, R.J.V., Barnes, J. (Eds.), Astronomical Data Analysis Software and Systems II, ASP Conference Series, vol. W2, p. 173–183.
West, R.A., Strobel, D.F., Tomasko, M.G., 1986. Clouds, aerosols and photochemistry in the jovian atmosphere. Icarus 65, 161–217.
Westphal, J.A., 1969. Observations of localized 5 micron radiation from jupiter. Astrophys. J. 157, L63–L64.
Wong, M.H., Mahaffy, P.R., Atreya, S.K., Niemann, H.B., Owen, T.C., 2004. Updated Galileo probe mass spectrometer measurements of carbon, oxygen, nitrogen, and sulfur on Jupiter. Icarus 171, 153–170.
Wong, M.H., de Pater, I., Marcus, P.S., Asay-Davis, X., Go, C.Y., 2010. Jupiter's Oval BA before and after it reddened: What changed? Icarus, in preparation.
Youssef, A., Marcus, P.S., 2003. The dynamics of jovian white ovals from formation to merger. Icarus 162, 74–93.